JOURNAL OF MATERIALS SCIENCE 26 (1991) 3086–3106

Thermal effects on the microstructure and mechanical properties of ion implanted ceramics

S. J. BULL*, T. F. PAGE‡
Department of Materials Science and Metallurgy, University of Cambridge, Pembroke Street, Cambridge CB2 3QZ, UK

The effects of varying the substrate temperature on the implantation-induced structures and surface mechanical properties of single crystal sapphire and MgO have been investigated for a range of 300 keV implanted ions. As the implantation temperature is lowered, the dose at which amorphization occurs is reduced and thus, for the same doses, more amorphous material is produced at lower temperatures. Quantitative modelling shows that the activation energy for annealing of the amorphous material during implantation is very much lower than might be expected for post-implantation thermal annealing of the same material. Also, as the implantation temperature increases there is a small amount of damage annealing in the damaged-but-crystalline material.

Both the microhardness and implantation-induced stresses depend critically on the presence of amorphous material since this is relatively soft and can support only small stresses. However, while the hardness behaviour in the damaged-but-crystalline material is dominated by radiation hardening, the substitutionality, ionic misfit and charge state of the implanted ions have also been found to contribute to the further solid solution component of the hardening produced by ion implantation. These effects are also observed to be temperature dependent.

Crazing of the implanted layers has also been reappraised. It has been established that the formation and configuration of crazes is a sensitive function of implantation temperature, and it is now proposed that crazes form in response to the stresses generated as a result of the thermal expansion mismatch between the amorphous layer and the substrate.

1. Introduction

Ion implantation is a clean, shallow, surface engineering technique whereby the mechanical, physical and chemical properties of a thin surface layer (typically $\leqslant 500$ nm thick) may be controllably altered. The effects of ion implantation on the surface mechanical properties of hard ceramic materials are now well documented (e.g. [1–6]) and the changes produced have been related to the microstructures and defect states that arise from the implantation process. For instance, implantation of sapphire to doses $\sim 10^{16}$ ions cm^{-2} results in surface hardening due to the effects of both the implanted ions (solid solution hardening) and the defects produced as they come to rest in the target (radiation hardening). An ion of energy ~ 100 keV may displace as many as 1000 target atoms from their structural sites in a ceramic material and thus radiation hardening dominates with solid solution hardening effects playing only a minor role [7]. The presence of these defects in the surface layer (and to a small extent the implanted atoms also) produces a volume expansion which generates a compressive residual stress in the implanted layer [6, 8, 9]. As the dose of implanted ions is increased, the number of defects increases and both the hardness and the implantation-induced stresses are also observed to increase. Significant increases in hardness ($\sim 50\%$ over unimplanted materials) and large compressive stresses ($\sim$ several GPa) are achievable in this way.

At a particular damage level (which corresponds to a particular dose for a given implanted ion–energy–target combination) both surface softening and some stress relief are, however, observed due to the amorphization of the target material [7, 8]. This amorphous layer initially forms below the surface, but grows with increasing implantation dose until it extends to the surface. At the dose when this occurs, the measured shallow-penetration hardness of the implanted material is usually less than that of the unimplanted substrate [1] and has been estimated to be 50 to 60%

* *Present address*: Materials Development Division, AEA Technology, Harwell, Didcot, Oxon, OX11 ORA, UK.
‡ *Present address*: Materials Division, Department of Mechanical, Materials and Manufacturing Engineering, Herschel Building, The University, Newcastle upon Tyne NE1 7RU, UK.

0022–2461/91 $03.00 + .12 © *1991 Chapman and Hall Ltd.*

of that of the unimplanted material for sapphire [4]. The presence of the implantation-induced stresses results in an apparent increase in the near-surface fracture toughness of the implanted material [6, 8] which manifests itself in the shortening of the radial crack traces around Vickers hardness impressions. Suppression of lateral crack formation and/or break out can also occur. On amorphization some stress relief occurs and this higher fracture toughness usually appears to decrease; however, these near-surface effects on toughness can be misleading if thought of as representing bulk properties.

Such changes in properties with implantation are generally found to extrapolate from model single crystal systems to polycrystalline ceramics for engineering applications though some further effects can be found in more complex microstructures and toughened materials (e.g. transformation-toughened zirconias) [10].

The occurrence of radiation damage controls radiation hardening, the generation of implantation-induced stresses, and the onset of amorphization. The extent of this damage, and hence its effects on these properties, will, however, depend on the specimen temperature during implantation since this would be expected to control the thermal component of damage annealing which can occur in addition to any dynamic (athermal) radiation annealing occurring during implantation. Currently there are some results to support this hypothesis; for example, for Ni-implanted (0 0 0 1) sapphire, Hioki *et al.* [6] reported that the dose for the onset of amorphization is reduced from $> 1 \times 10^{17}$ $Ni^+ cm^{-2}$ at room temperature to 2×10^{15} $Ni^+ cm^{-2}$ for implantation at 100 K. Similar observations have been made for other systems [5].

The implantation of heavy ions into some ceramic substrates has been observed to cause a number of surface topography changes including crazing of the surface [2, 11]; crazes appearing as cracks which open up in the surface layer at some point during the implantation process. These crazes have been found to occur only when an amorphous surface layer is present, the crazes extending from the surface through the amorphous layer to the damaged by crystalline material beneath. The detailed mechanisms for the formation of these crazes have, however, been unclear apart from the suggestion that tearing of the amorphous layer occurs probably in response to bending stresses.

In this paper we report the results of a systematic study of the effects of varying the substrate temperature during implantation for two model single crystal systems (sapphire and MgO). Temperature-sensitive changes in surface structure have been correlated with observed changes in hardness and stress state. A new cause for the previously observed crazing phenomenon is also proposed, based on observations of yttrium-implanted sapphire at a range of substrate temperatures.

2. Experimental procedure

2.1. Ion implantation

Semiconductor substrate single crystal sapphire wafers of $\{1\,0\,\bar{1}\,2\}$ orientation were supplied with one side prepolished to a good finish (courtesy of GEC Wembley). These were cleaved into sections of size $25 \times 25 \times 0.4$ mm^3 and carefully ultrasonically cleaned and degreased in alcohol. High purity single crystal (0 0 1) habit MgO (W&C Spicer, London) was cleaved along (1 0 0) into $10 \times 5 \times 1$ mm^3 sections and cleaned and degreased as for the sapphire samples. The MgO specimens were then mounted on to stainless steel discs and tilted a few degrees off the $\langle 0\,0\,1 \rangle$ axis to reduce the effects of channelling during implantation. These two substrates are known to have different post-implantation annealing characteristics with damage annealing at lower temperatures in MgO ($\sim 800\,^\circ C$) than in sapphire ($\sim 1100\,^\circ C$) [12, 13].

The specimens were then implanted with Ti^+, Y^+ or Cr^+ ions of 300 keV energy in the Cockcroft–Walton facility at UKAEA Harwell. The ions were chosen because they are known to give different damage levels and chemical behaviour after implantation [8, 11–13]. Five different implantation temperatures were chosen covering the full range that the specimen holder in the chamber of the Cockroft–Walton implanter could produce. Liquid nitrogen cooling was used to achieve target temperatures of 150 and 300 K and a combination of this and radiative heating was further used to maintain the specimens at 473, 673 and 760 K. These background temperatures could be controlled to an accuracy of $\pm$ 10 K. Details of the target chamber can be found elsewhere [14].

Though the specimen temperature was set and allowed to equilibrate before implantation, it could not be maintained once implantation started due to the highly localized effects of beam heating. Implantations were carried out with a beam current of 2 $\mu A\,cm^{-2}$ which, for an accelerating voltage of 300 kV, gives a beam power of 0.6 $W\,cm^{-2}$. Since good thermal contact between the specimen and its carousel holder cannot be routinely guaranteed, the specimen mainly loses heat by radiation. This has been confirmed experimentally (e.g. [14, 15]). Thus, the rate of temperature rise in the specimen will be controlled by the difference between the beam power and the radiative heat loss [15], i.e.

$$\frac{dT}{dt} = \frac{P - \varepsilon\sigma(T^4 - T_0^4)}{Sd\delta} \qquad (1)$$

where T is the specimen temperature, T_0 the temperature of the surroundings, P the beam power density, σ Stefan's constant, S the specific heat of the substrate, d the substrate thickness, δ the substrate density and ε the fractional radiative efficiency (usually determined by experiment and taken to be 1 in the argument which follows). The time increment dt may be converted into a dose increment $d\Phi$ by

$$d\Phi = \frac{I\,dt}{e} \qquad (2)$$

where I is the beam current and e the charge on the electron. Fig. 1 shows the computed temperature rise with dose for sapphire implanted at all the starting temperatures used in this study. The temperature rise

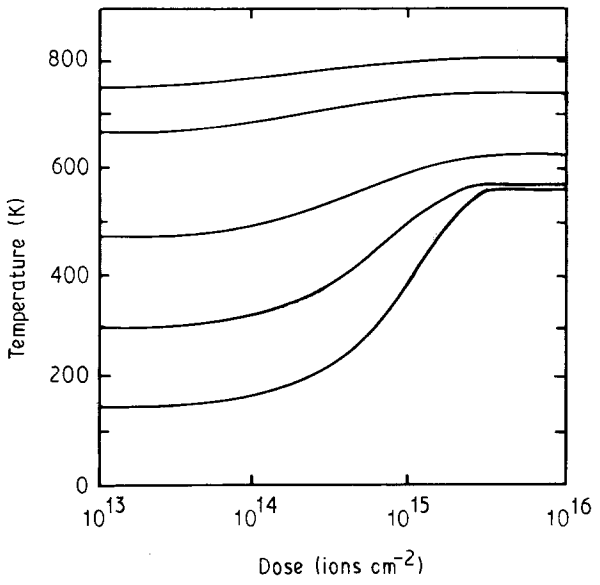

Figure 1 The calculated temperature rise during implantation for sapphire for a range of starting temperatures assuming heat loss by radiation only. The temperature rise for specimens held at room temperature is $\approx 250\,°C$. Above 5×10^{15} ions cm^{-2} the specimen has reached equilibrium temperature. $I_b = 2\,\mu A\,cm^{-2}$, $E = 300\,kV$.

due to beam heating reaches a maximum at doses less than 1×10^{16} ions cm^{-2} which is the lowest dose investigated for sapphire in this study. The final temperature of the specimen occurs when $dT/dt = 0$ which may be calculated (by rearranging Equation 1) by

$$T = \left(\frac{P}{\sigma} + T_0^4\right)^{1/4} \quad (3)$$

Table I shows both the final temperatures and the temperature rises for all the specimens implanted in this study. In practice, the rate of temperature rise for MgO was slightly greater than for sapphire due to the smaller thermal masses of the specimens used.

Obviously, some heat will be lost to the implantation chamber by conduction, and thus these values may be regarded as the maximum possible temperature rises. In practice, temperature measurements from thermocouples in contact with a sample implanted at room temperature to a dose of 2.5×10^{16} Ti^+ cm^{-2} show a temperature rise of only $\sim 125\,°C$ during implantation which is about half the value calculated from the above approach. On the other hand, the heat generated by the implanted ions as they come to rest at the end of their trajectories in the target will produce "thermal spikes" beneath the surface and thus heat must be transferred to the surface (and into the bulk) by thermal conduction in the substrate in order that it be lost to the target chamber by radiation. Since the damage produced in the implantation process will reduce the thermal conductivity of the implanted layer, the temperature in this layer may well be somewhat higher than the bulk target temperature. Such temperature differences are, however, probably small compared to the bulk temperature rise. The Table I values can thus be taken as reasonable upper bounds for the temperature rise on implantation.

TABLE I Maximum specimen temperature rises on implantation for MgO and sapphire (300 kV ions at $2\,\mu A\,cm^{-2}$) as calculated from Equation 3. T_0 is the background temperature of the specimen holder while T is the maximum equilibrium temperature created by beam heating.

Temperature		Temperature rise $T-T_0$ (K)
T_0 (K)	T (K)	
150	571	421
300	581	281
473	628	155
673	747	74
760	814	54

Three implantation doses were chosen with respect to the known room temperature implantation behaviour (see Table II). These were selected to produce a damaged-but-crystalline layer, a subsurface amorphous layer and a surface amorphous layer for implantation at 300 K. The doses were measured with a Faraday cup arrangement and checked by post-implantation Rutherford Backscattering (RBS) using the IBIS 3 MeV Van der Graaf at UKAEA Harwell. For the lower dose implants, good agreement was found between the Faraday cup dose and that determined by RBS. At higher doses there was a bigger difference between the two, but a reasonable agreement was maintained between specimens implanted to the same dose at different temperatures. At these doses, the RBS measurements were less than the Faraday cup values implying that charging of the specimen during implantation had resulted in some beam deflection and subsequent reduction of the implanted dose.

Table III shows a summary of the ion–energy–substrate combinations used in this study, together with the range and damage parameters and the energy deposited in displacement collisions per ion as calculated by a modified version of the EDEP-1 computer code [16].

2.2. Surface characterization

A number of techniques were used to determine whether the implantations had resulted in amorphization of the substrate. For those specimens implanted at room temperature, a channelled Rutherford backscattering (RBS) technique was employed as described previously [2]. In addition, both transmission and scanning electron microscopy methods (TEM and SEM) were used to investigate the damage state of the surface. In the SEM, the disappearance of electron channelling contrast (ECP) in the implanted region was used as evidence that the amorphous layer extends to (or at least close to) the surface. According to Joy *et al.* [17] the channelling contrast arises from the top ~ 100 nm of the sample and this has also been confirmed by Page *et al.* during detailed SEM channelling studies of ion-implanted sapphire [18]. In the TEM, electron diffraction was used on specimens carefully back-thinned and then briefly thinned from both faces to allow diffraction patterns to be determined from the subsurface region. The replacement of

TABLE II Dose–substrate combinations investigated together with the expected room temperature surface structures produced by ion implantation.

Ion	Substrate	Doses		
		Damaged but Crystalline (ions cm^{-2})	Subsurface amorphous (ions cm^{-2})	Surface amorphous (ions cm^{-2})
Ti	Al_2O_3	2.5×10^{16}	1×10^{17}	7×10^{17}
Y	Al_2O_3	1.1×10^{16}	9.9×10^{16}	8.5×10^{17}
Ti	MgO	1×10^{14}	1×10^{16}	1×10^{17}

TABLE III Range and damage parameters for the materials implanted in this study as determined by the modified EDEP-1 Code [16]. R_p and ΔR_p describe the range and large-straggling while X_d and ΔX_d similarly describe the damage distribution. E_c is the energy per incident ion dissipated as displacement damage.

Target	Ion	E_0 (keV)	R_p (μm)	ΔR_p (μm)	X_d (μm)	ΔX_d (μm)	E_c (keV ion^{-1})
Sapphire	Ti	300	0.143	0.041	0.088	0.051	125
	Y	300	0.081	0.023	0.046	0.028	152
	Cr	300	0.130	0.038	0.080	0.047	131
MgO	Ti	300	0.153	0.043	0.094	0.054	125

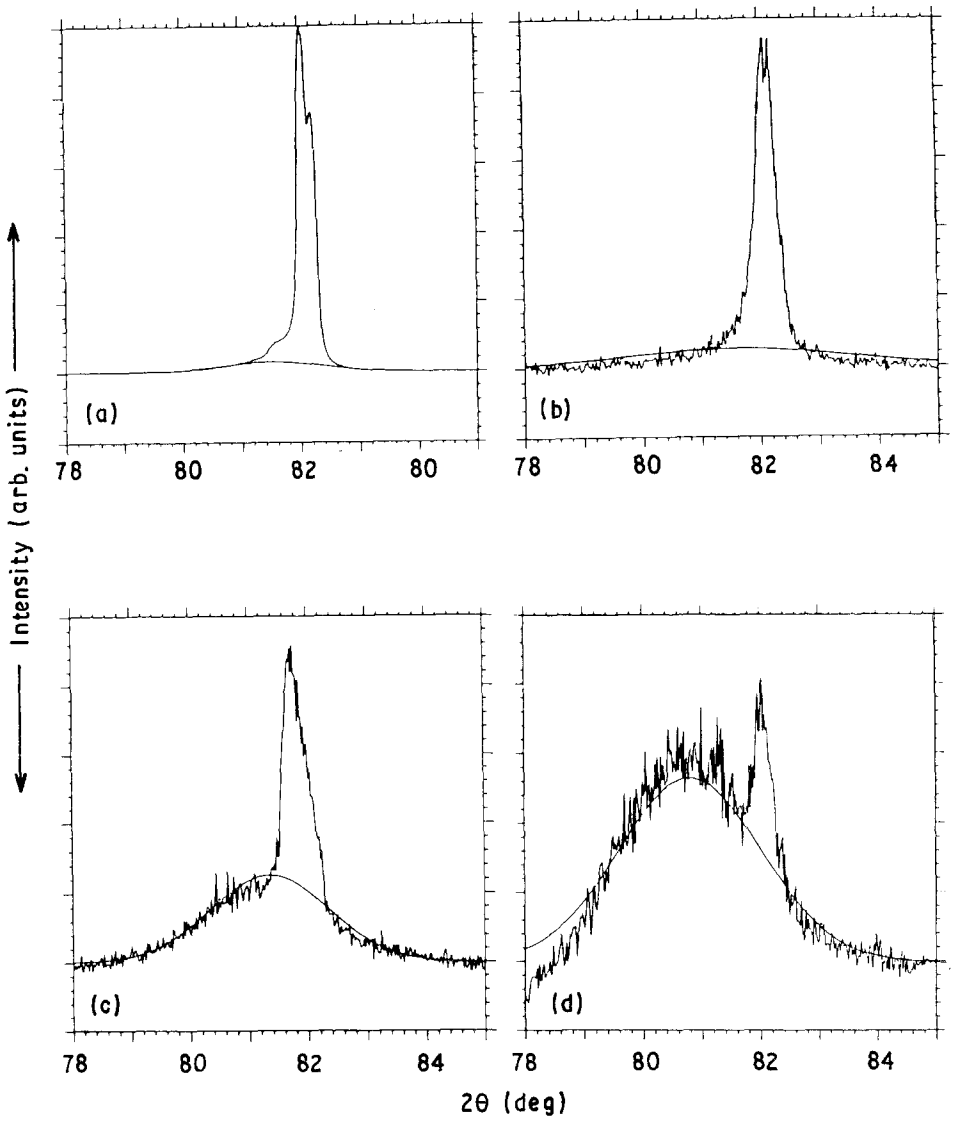

Figure 2 X-ray peak profiles of the $(20\bar{2}4)$ reflection in Ti-implanted $(10\bar{1}2)$ sapphire (a) 1×10^{16} Ti^+ cm^{-2} (b) 5×10^{16} Ti^+ cm^{-2} (c) 1×10^{17} Ti^+ cm^{-2} (d) 5×10^{17} Ti^+ cm^{-2}. The sharp peak in the low dose implanted material (showing resolved K_{α_1}, and K_{α_2} peaks) is replaced by a broader, more diffuse peak as the dose of Ti is increased. On amorphization a broad Gaussian hump centred on a slightly lower (2θ) angle (hence a higher *d*-spacing) is formed.

the normal diffraction pattern with a number of diffuse rings was used as evidence that amorphization had occurred below the surface. Finally, as a check for the other techniques, X-ray diffraction peak profiles of the $(2\,0\,\bar{2}\,4)$ reflection were obtained using low penetration CrK_α radiation. Sharp peaks were produced in the damaged but crystalline material, whereas a more Gaussian spread is superimposed on this once amorphization has taken place (see Fig. 2). In some cases where a thick surface amorphous layer is produced, only the broad Gaussian peak is observed. This was particularly apparent at low implantation temperatures.

2.3. Indentation analysis

Knoop and Vickers microhardness tests were performed with a Leitz Miniload 2 microhardness tester. All indentations were made under standard conditions (ambient temperature, humidity 50% to 80%, laboratory air, 15 s dwell time) with indenter diagonals carefully aligned with known crystallographic directions to minimize the potential effects of hardness anisotropy. For $(1\,0\,\bar{1}\,2)$ sapphire specimens the long Knoop diagonal or one of the Vickers diagonals was aligned with $[2\,1\,\bar{1}\,0]$. For (0 0 1) MgO a similar alignment was made with [1 0 0]. To follow the changes in surface hardness, low load Knoop indentations were used with loads in the range 10 to 50 gf (1 gf = 9.8 $\times 10^{-3}$ N) where the majority of the plastic zone associated with the indentation is expected to lie in the implanted layer. Five indentations were performed at each load. For the comparisons to be made here, it was not felt necessary to further deconvolute the Knoop hardness by the composite hardness models of Burnett and Page [2].

For measuring the changes in surface stress state in sapphire, the changes in the lengths of the radial cracks around Vickers indentations at loads of 100 and 500 gf were used. Burnett and Page [2] have given a detailed description of the cleavage crack geometries around indentations for $(1\,0\,\bar{1}\,2)$ sapphire. In the present study, only the well developed $\langle\bar{0}\,2\,2\,1\rangle$ traces of the $(1\,\bar{0}\,1\,2)$ cracks were measured since the other crack systems probably have a different work of fracture. Cracks ending unusually close to the indentation or showing significant branching were ignored. In all cases, sufficient indentations were performed so as to obtain 20 crack measurements. All measurements (both crack lengths and indentation diagonals) were made with the optical system of the microhardness tester.

For the specimens that produced well developed radial cracks, the difference in radial crack length between the implanted and unimplanted material was used to determine the integrated surface stress, S, using the following relationship of Lawn and Fuller [19]. The integrated surface stress, S, can be determined from

$$1 - (C_0/C)^{3/2} = \frac{2\psi S}{K_c d^{1/2}} \quad (4)$$

where C_0 is the crack length in unstressed material, C the crack length in the implanted specimen, ψ a constant (generally taken to be unity [19]), K_c the local unstressed fracture toughness (a value determined from the indentation cracks in unimplanted material and calculated using the formulation of Anstis *et al.* [20] was used in this study), and d the thickness of the stressed layer (assumed to be equal to $4\Delta X_d$) where ΔX_d is the range straggling from the EDEP-1 analysis. This technique is known to underestimate the stresses by a factor of 6 to 10 but shows the correct trends with implantation dose [8].

3. Results and discussion

3.1. Implantation-induced amorphization

3.1.1. Observations

Table IV shows the crystalline–amorphous nature of all the Ti-implanted sapphire specimens implanted in this study, together with the methods used to determine whether the surface layer was crystalline or amorphous. All implantations carried out at 150 K produced amorphous layers extending to the surface. As the temperature was increased, the amount of amorphous material decreased until, by 760 K, only the highest dose implantation rendered any part of the substrate amorphous. This behaviour can be seen

TABLE IV The surface structure of Ti-implanted sapphire as determined by SEM electron channelling patterns (ECP), X-ray diffractometry (XRD), transmission electron microscopy (TEM) and Rutherford Backscattering (RBS). A = Amorphous; C = Damaged but crystalline.

Temperature (K)	Dose (ions cm^{-2})		
	2.5×10^{16}	1×10^{17}	7×10^{17}
150	A (ECP, XRD)	A (ECP, TEM)	A (ECP, TEM)
300	C (ECP, XRD, RBS)	A (ECP, RBS)	A (ECP, XRD, RBS)
473	C (ECP, XRD)	A (ECP)	A (ECP, XRD)
673	C (ECP, XRD)	A (ECP, TEM)	A (ECP, XRD)
760	C (ECP, XRD)	C (ECP, TEM)	A (ECP, XRD)

from the electron channelling patterns for the specimens implanted to 2.5×10^{16} Ti^+ cm^{-2} at 150, 300 and 760 K (Fig. 3a to c). The pattern for the specimen implanted at 150 K is completely degraded in the implanted region, whereas, above this temperature, the strong channelling lines in the patterns are still visible. It can thus be concluded that the surface has been amorphized at 150 K but at temperatures above this it is still damaged but crystalline. Fig. 3d to f shows the electron channelling patterns for sapphire implanted with 1×10^{17} Ti^+ cm^{-2} at these same temperatures. In this case, the two lower temperature implantations can be seen to have produced amorphous material whereas the 760 K implant has left the larger surface crystalline. No evidence for surface crystallinity was found for any of the specimens implanted to 7×10^{17} Ti^+ cm^{-2}.

Table V shows the crystalline–amorphous data for Y-implanted sapphire. Since yttrium is a heavier ion it creates more displacements and, consequently, the amorphization dose is lower at room temperature. The behaviour with temperature is similar to the Ti-implanted case. At 150 K, all specimens are rendered amorphous by ion implantation, whereas, at temperatures above this, the dose at which amorphization starts is increased. At 760 K it is still less than 1×10^{17} Y^+ cm^{-2}.

3.1.2. Modelling the amorphization process

In order to model the development of amorphous material, it is important to consider how this might be produced from the damage caused by the implantation of energetic ions. According to Morehead and Crowder [21], amorphization occurs by the overlapping of the displacement spikes caused by single implanted ions. For heavy ions ($Z \gtrsim 5$), these are readily considered to have amorphous cores and it is possible to postulate that a discrete amorphous layer will be formed when these amorphous cores overlap (allowing for the effects of any annealing (be it thermal or radiation-enhanced)). Amorphization has, however, also been observed to occur for light ions ($Z \lesssim 5$) whose displacement spikes are not believed to have amorphous cores and so this model may not be sufficient to explain the amorphization phenomenon for all ion–energy–substrate combinations. In the case of light ions, amorphization occurs by the progressive overlap of several displacement spikes in order to build up sufficient damage and is thus a much more complex process. All the ions implanted in this study may, however, be regarded as "heavy" and we will not consider the case of light ions further.

So far, we have referred to the "amorphous" state as if it is a single-phase, glassy-structured material. Whilst this is a useful concept, especially in terms of assigning properties (e.g. hardness and strength) to the apparently structureless states which can be produced by severe implantation, it is probably misleading as a

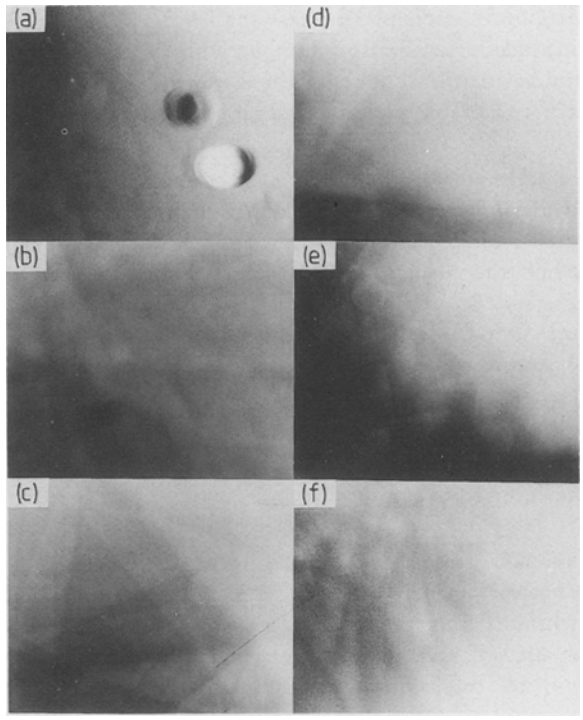

Figure 3 Wide area channelling patterns obtained in an SEM at 30 kV across the implanted–unimplanted boundary for $(10\bar{1}2)$ sapphire implanted to (a) 2×10^{16} Ti^+ cm^{-2} at 150 K (b) 2.5×10^{16} Ti^+ cm^{-2} at 300 K (c) 2.5×10^{16} Ti^+ cm^{-2} at 760 K (d) 1×10^{17} Ti^+ cm^{-2} at 150 K (e) 1×10^{17} Ti^+ cm^{-2} at 300 K and (f) 1×10^{17} Ti^+ cm^{-2} at 760 K. For implantation at 150 K the pattern is completely degraded in the implanted region indicating the presence of an amorphous layer extending to the surface. Higher temperature implants are still crystalline at the lower dose whereas at 1×10^{17} Ti cm^{-2} the pattern is completely degraded at both 150 and 400 K, but not at 760 K, indicating that the surface layer is crystalline at the highest temperature.

TABLE V Surface structures of Y-implanted sapphire (see Table IV for terminology).

Temperature (K)	Dose (ions cm^{-2})		
	1.1×10^{16}	9.9×10^{16}	8.5×10^{17}
150	A (ECP, XRD)	A (ECP, TEM)	A (ECP, XRD)
300	C (ECP, XRD, RBS)	A (ECP, RBS)	A (ECP, XRD, RBS)
473	C (ECP, XRD)	A (ECP, TEM)	A (ECP, XRD)
673	C (ECP, XRD)	A (ECP, TEM)	A (ECP, XRD)
760	C (ECP, XRD, TEM)	C (ECP, XRD, TEM)	A (ECP, XRD)

structural concept. Firstly, the "amorphous" states produced by radiation damage with different ions are almost certainly chemically different and may be structurally dissimilar especially if the implanted species itself plays a key role in creating flexible linkages between the structural units of the substrate (by analogy, playing the part of the modifying ions in silicate glasses). There is a further sense, however, in which the implanted species is important and that concerns the absolute scale and surface-to-volume ratio of the displacement spikes produced during implantation. While it is useful to think of the "amorphous" state as resulting from the spatial overlap of these spikes, such a concept would have to include the possibility of radiation annealing occurring whereby the interstitials predominantly around the periphery of one spike may structurally relocate in nearby vacancies as another spike passes through them. Some genuine thermal annealing might also be expected around the periphery of each spike, but this effect will be less marked in the spike centres where vacancies tend to predominate over interstitials. We would therefore expect the structure of the state described as "amorphous" to be varying rapidly from point to point both in and between the displacement spikes: that is with varying degrees of disorder ranging from "truly amorphous but highly defective material" to "damaged but nearly crystalline material" existing in close proximity. We believe that we have some evidence of this phenomenon in the substitutionality–annealing aspects of the solid solution effects reported in the next section.

The "amorphous" state thus probably depends on the implant species used, on the damage distribution in each spike, on the level of radiation annealing occurring as the spikes overlap, on the geometry of each spike particularly in terms of the interstitial–vacancy population and on general thermal annealing effects (though such effects will be complicated by the thermal spikes introduced into the material during the radiation damage process). While this state of affairs sounds complicated, it reflects the situation thought to exist in the radiation damage literature of the late 1960s (e.g. [14]) and it is still difficult to refine these concepts and models further.

From our observations it is possible to estimate the temperature variation of the minimum dose, Φ_{crit}, at which amorphization starts beneath the surface using the model of Morehead and Crowder [21]. These workers derived the relationship

$$\Phi_{crit} = \Phi_0[1 - K(dE/dx)_0^{1/2} \exp(-U/kT)]^{-2} \quad (5)$$

relating the initial energy loss in displacement collisions $(dE/dx)_0$ to the final damage state, where K is a measure of the damage efficiency of the implanted ion (and is related to the damage cascade for each collision), U the activation energy for annealing of the amorphous material and Φ_0 the dose at which all target atoms have been displaced by primary collisions. Assuming that amorphization occurs when all target atoms have been displaced in a particular region [21]

$$\Phi_0 = E_d N(dE/dx)_0^{-1} \quad (6)$$

where E_d is the target atom threshold displacement energy, N the number of atoms per unit volume and $(dE/dx)_0$ the initial displacement energy loss rate given by

$$(dE/dx)_0 = 7 \times 10^8 \delta Z_1^{2/3} M_1(M_1 + M_2) \quad (7)$$

where M_1 and Z_1 are the mass number and atomic number of the ion, M_2 is the mass number of the target and δ the target density. Equation 6 will only give an approximate value for Φ_0 and a better determination could be made by performing a three-parameter-fit to Equation 5 for Φ_0, K and U. This requires, however, a larger number of amorphization dose–temperature combinations than was possible in this study, but approximate values can be estimated from our data as follows.

For the Y-implanted sapphire, the amorphization dose at 300 K (as determined by RBS) was found to be $\sim 3 \times 10^{16}$ Y^+ cm^{-2} (300 keV) which is in good agreement with the results of Burnett and Page [2]. For the 300 keV Ti-implanted sapphire, the amorphization dose at 300 K is 8×10^{16} Ti^+ cm^{-2} but this rises to $\sim 2 \times 10^{17}$ cm^{-2} at 760 K. Table VI shows the amorphization single-dose–temperature combinations fitted to Equation 5, together with the simple fitted values of K and U and the calculated value of Φ_0. Values of the annealing energy, U, for the two ions are seen to be comparable since small changes in U do not have a significant effect on the dose–temperature behaviour. Based on this observation, a reasonable average value of 0.0018 eV (the average of the fitted U values) may be used to predict the amorphization dose at a given temperature and still give a reasonable fit to experimental data (Fig. 4a). The value of the annealing

TABLE VI Morehead and Crowder fitting parameters for sapphire and MgO. Φ_{crit} is the minimum dose at which amorphization of the substrate is observed.

Ion	Substrate	T (K)	Φ_{crit} (ions cm^{-2})	Φ_0 (ions cm^{-2})	K (keV $cm^{-1})^{1/2}$	U (eV)
Ti	Sapphire	300	8×10^{16}	3.40×10^{14}	126	0.0013
		760	2×10^{17}			
Y	Sapphire	300	2.8×10^{16}	2.93×10^{14}	177	0.0022
		760	6×10^{16}			
Ti	MgO	300	8.5×10^{16}	2.08×10^{14}	118	0.0012
		473	1×10^{17}			

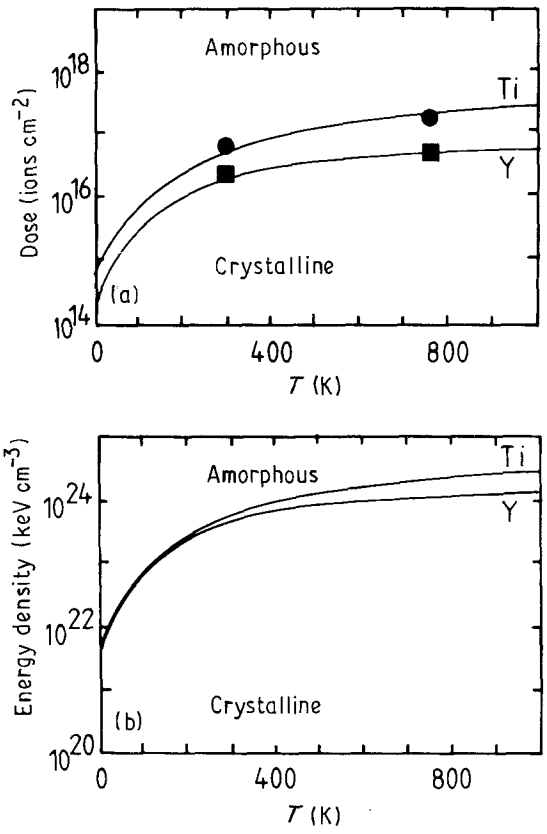

Figure 4 (a) Fits of the Morehead and Crowder amorphization model to experimental data for Ti and Y-implanted (1 0 $\bar{1}$ 2) sapphire using an annealing energy value of 0.0018 eV (determined by taking the average of the best fit values for the two different ions). The model predicts that implantation at 150 K will produce amorphous material for all specimens implanted to doses $> 1 \times 10^{16}$ which is observed. (b) The same fitted lined replotted in terms of damage energy density. At low temperatures the damage annealing rates (and hence the amorphization doses) are nearly equivalent for the two ions. At higher temperatures, the higher damage densities created by the heavier ion result in the critical amorphization energy being lower for Y (as observed by Burnett and Page [1]).

energy is very much smaller than that obtained for silicon by Morehead and Crowder ($U = 0.06$ eV [21]) which is not surprising since in predominantly covalent materials there is expected to be only a small amount of *in situ* annealing of amorphous material (e.g. [3]). Both these activation energies are much smaller than the activation energies for thermal annealing of defects in these materials (typically ~ 5 eV [22]) showing the importance of the "thermal spike" and the high damage concentration on the diffusion properties during implantation. Essentially, these low energies reflect the lack of thermal sensitivity of these effects rather than allowing any specific processes to be identified.

The values of K are less comparable since small changes in K produce large variations in the amorphization dose against temperature curve. The function of the constant K is to relate the final damage state before annealing to the initial energy loss in displacement collisions and, as such, it takes into account those defects produced in secondary collisions. Since Y is a heavier ion than Ti, it transfers more energy to any target atom during knock-on and thus more secondary collisions are produced. The value of K will thus be larger than for Ti, as is observed, though given the accuracy of the curve fitting it is difficult to make any further inferences about this.

Perhaps a more useful way to predict the onset of amorphization is to use the critical energy deposition criteria for amorphization (CECA) approach [1, 23–25]. In this model, once a critical amount of displacement damage has been created by ion implantation the target will be amorphized but allowance has to be made for dynamic annealing effects etc. The particular damage level at which amorphization occurs and the effects of damage annealing on this are however not amenable to simple calculation but it has been established that the local energy dissipated in displacement collisions at the amorphization dose reflects the overall results of these processes and can be used as a criterion for predicting the onset of amorphization. This criterion is essentially independent of ion energy. According to the model of Burnett and Page [1], amorphization will initially occur at the peak of the Gaussian damage profile below the surface and the critical damage energy deposition at this point (ρ_{CECA}) is given by

$$\rho_{CECA} = \frac{\Phi_{crit} E_c \times 10^4}{(2\pi)^{1/2} \Delta X_d} \quad (8)$$

where E_c is the energy per incident ion lost in displacement damage processes. For given ion–substrate–input energy combinations, E_c can be calculated using a number of currently available computer codes describing the collision processes (e.g. [16]). By combining Equation 8 with Equation 5 the variation of amorphization dose with temperature may be converted to the variation of ρ_{CECA} with temperature, $\rho_{CECA}(T)$ by

$$\rho_{CECA}(T) = \rho^{\circ}_{CECA}[1 - K(dE/dx)_0^{-1/2} \exp(-U/kT)]^{-2} \quad (9)$$

where ρ°_{CECA} is the energy deposition for all substrate ions to be displaced by primary collision. Fig. 4b shows plots of ρ_{CECA} against temperature calculated from the data in Fig. 4a. At very low doses the energy deposition required for amorphization is the same for both ions since the effects of annealing are not significant. As the temperature increases the behaviour is observed to diverge; amorphization of sapphire by titanium requires a larger energy deposition than amorphization with yttrium. This behaviour was also observed by Burnett and Page [8] for room temperature implants in sapphire. These workers quote ρ_{CECA} (3 0 0) as 8×10^{23} keV cm^{-3} for Ti-implanted sapphire and 6×10^{23} keV cm^{-3} for Y-implanted sapphire, both of which are close to the values determined in this study. The fact that the damage produced by Y-implantation occupies a much smaller volume than for Ti-implantation might allow stable defect complexes to form whilst the displacement spike is still "hot" and thus the amount of damage–annealing would be reduced. This could explain the difference between the two curves, but the detailed damage recovery mechanisms in the two cases are as of yet unknown.

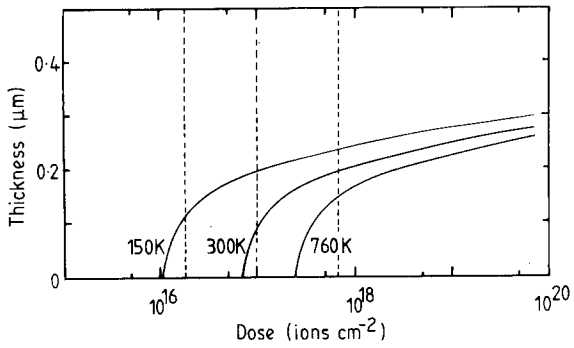

Figure 5 Variation of the thickness of the amorphous layer formed by Ti implantation of (1 0 $\bar{1}$ 2) sapphire, with doses for the range of implantation temperature used in this study. The thickness was calculated using the model of Burnett and Page [1]. Increasing the implantation temperature increases the dose at which amorphization starts, but does not change the form of the thickness–dose curve. The vertical dotted lines mark the three doses investigated in this study.

Changing the temperature to change the dose at which the onset of amorphization occurs is also expected to change the spatial distribution of damage annealing and thus change the thickness and position of the amorphous layer beneath the surface. Fig. 5 shows the thickness against dose behaviour for Ti-implanted sapphire calculated from the model of Burnett and Page [1] for implants at 150, 300 and 760 K. Changing the amorphization dose shifts the curve along the dose axis, but does not affect its shape. As the temperature is increased – and the dose at which amorphization starts is also increased – the thickness of the amorphous layer produced at a much higher dose will thus be reduced until it eventually disappears. This change in amorphous layer thickness, together with the fact that the same specimens may have completely recrystallized, will have a major effect on the mechanical properties of these specimens (see next section).

For the MgO specimens implanted over the same temperature range, similar behaviour to the sapphire implants was observed. Table VII shows the doses and temperatures used, together with the crystalline or amorphous nature of the implanted layers. At 150 K, amorphous layers were produced on the specimens implanted to 1×10^{16} Ti^+ cm^{-2} or higher. Above this temperature, neither of the two lower doses rendered the surface amorphous and implantation to 1×10^{17} Ti^+ cm^{-2} could only produce amorphization up to 473 K. At room temperature this material amorphizes at 8.5×10^{16} Ti^+ cm^{-2} under these implantation conditions. This is very similar to the behaviour observed for Ti-implanted sapphire. Indeed the fitted Morehead and Crowder parameters (Table VI), K and U, are almost identical to the sapphire case though the value of Φ_0 is somewhat lower. Somewhat surprisingly, this evidence suggests that the annealing behaviour is fairly independent of the structure of the target, but is more dependent on the damage produced by the implanted ion. A more comprehensive study is obviously needed to fully understand the mechanisms by which the amorphous material produced by ion implantation is annealed during the implantation process, though the necessary experimental approaches will probably have to be both difficult and indirect.

3.2. Mechanical properties

3.2.1. Microhardness

3.2.1.1. Experimental observations. The variation in damage and amorphization behaviour detailed in the previous section manifests itself in changes in the microhardness behaviour with implantation temperature. Fig. 6 shows the variation of Knoop hardness with implantation temperature for the Ti-implanted sapphire specimens. At 150 K, the 2.5×10^{16} Ti^+ cm^{-2} implanted specimen is much softer than at any higher temperature. This is because this specimen has been amorphized whereas the higher temperature implants remain crystalline. The fact that the measured hardness at 150 K is less than that of the unimplanted material implies that the amorphous layer extends to the surface. For the specimens implanted to 1×10^{17} Ti^+ cm^{-2} the hardness increases with implantation temperature reflecting the decreasing amorphous layer thickness as the temperature is increased; the thickness is maximum at 150 K, falling to zero by 760 K. Comparison with the hardness of unimplanted sapphire indicates that a surface amorphous layer is formed for implantation at 150 and 300 K and a subsurface amorphous layer at temperatures above this. Similar behaviour is observed for the 7×10^{17} Ti^+ cm^{-2} implants, though changes in the

TABLE VII Surface structure of Ti-implanted MgO (see Table IV for terminology).

Temperature (K)	Dose (ions cm^{-2})		
	1×10^{14}	1×10^{16}	1×10^{17}
150	C (ECP, XRD)	A (ECP, XRD, TEM)	A (ECP, XRD)
300	C (ECP, XRD, RBS)	C (ECP, XRD, RBS)	A (ECP, XRD, RBS)
473	C (ECP, XRD)	C (ECP, XRD)	A (ECP, XRD)
673	C (ECP, XRD)	C (ECP, XRD)	C (ECP, XRD)
760	C (ECP, XRD)	C (ECP, XRD)	A (ECP, XRD)

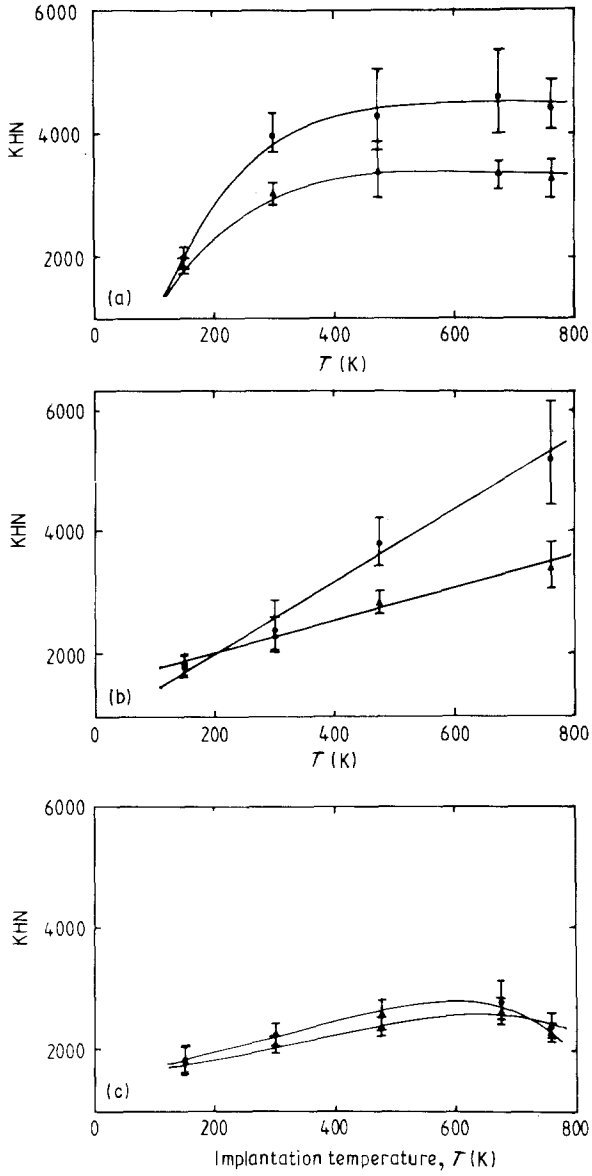

Figure 6 Variation of microhardness with implantation temperature for (a) 2.5×10^{16} Ti^+ cm^{-2} (b) 1×10^{17} Ti^+ cm^{-2} and (c) 7×10^{17} Ti^+ cm^{-2} implanted $(1\,0\,\bar{1}\,2)$ sapphire. For the lowest dose implant the specimen has been amorphized at 150 K and shows a lower hardness than at higher temperatures where the hardness is almost constant. For the higher dose specimens the hardness increases with temperature as the amorphous layer is progressively reduced in thickness. (● 25g, ▲ 50 g).

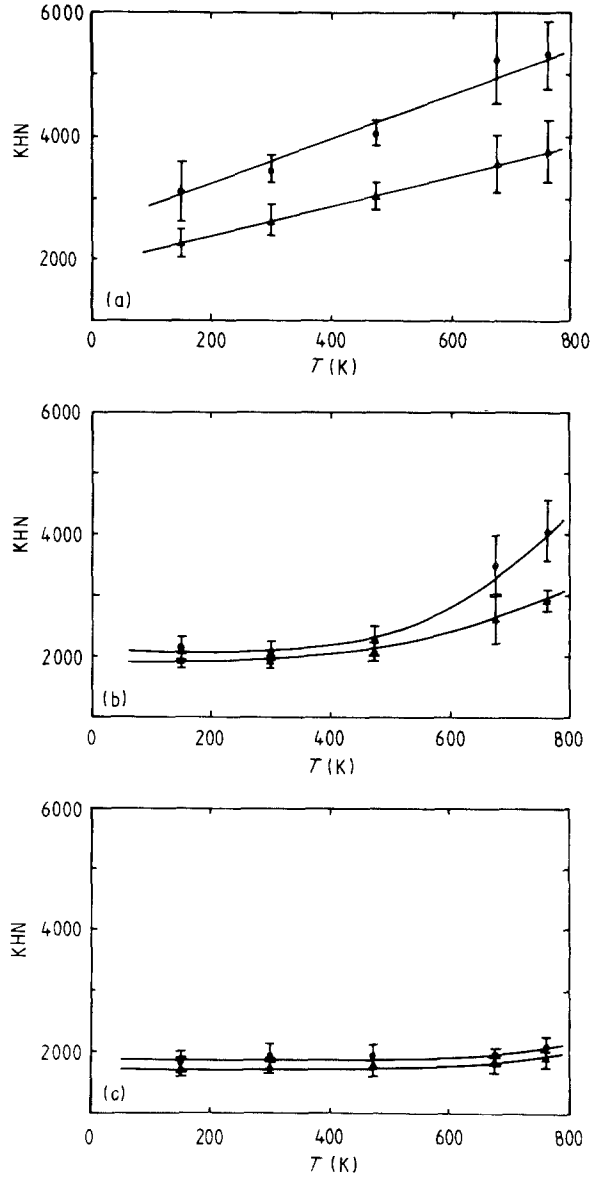

Figure 7 Variation of microhardness with temperature of implantation for (a) 1.1×10^{16} Y^+ cm^{-2} (b) 9.9×10^{16} Y^+ cm^{-2} and (c) 8.5×10^{17} Y^+ cm^{-2} implanted $(1\,0\,\bar{1}\,2)$ sapphire. As with the titanium implants the hardness increases as the amorphous layer thickness is reduced with increasing temperature. There is also, however, an increase in hardness with temperature at 1.1×10^{16} Y^+ cm^{-2} where no amorphous material is present. (● 25 g, ▲ 50 g).

thickness of the more extensive amorphous layer produced by implantation beyond this dose have a smaller effect on the measured hardness.

The hardness behaviour of the Y-implanted sapphire is shown in Fig. 7. For a dose of 1.1×10^{16} Y^+ cm^{-2} the hardness increases with implantation temperature. The hardness at 150 K is very close to the hardness of the unimplanted material implying that the amorphous material extends to close to the surface. At higher temperatures the implanted layer is damaged but crystalline. For 9.9×10^{16} Y^+ cm^{-2} the hardness is constant over the whole temperature range implanted here due to the formation of a thick surface amorphous layer which is not significantly altered by changes in the implantation temperature in any given material. This implies that the amorphous structures produced in these cases are essentially mechanically similar and thus probably independent of exactly how they were made.

Care is necessary when making indentations in Y-implanted sapphire at doses where amorphization has occurred due to the formation of surface crazes. In this case it is important that the indentations be placed in the material between the crazes for greatest accuracy. The crazing phenomenon is discussed in Section 3.3.2.

The importance of amorphization on the measured hardness is shown more clearly in Fig. 8 where hardness is plotted against dose for 25 gf indentations. For the Ti-implant the hardness increases from a relatively constant value at 150 K due to the removal of amorphous material. At intermediate temperatures the hardness decreases with increasing dose as expected from the chosen doses. At 760 K the

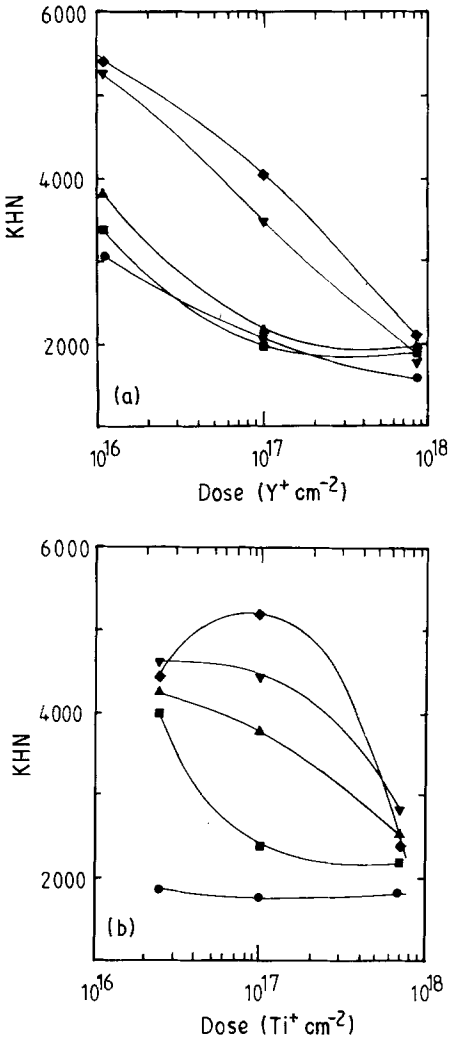

Figure 8 Variation of 25 g Knoop microhardness with dose for (a) Y-implanted (1 0 $\bar{1}$ 2) sapphire for all the temperatures investigated in this study. The hardness decreases with increasing dose for all but the highest temperature Ti-implants. This is due to the presence of soft amorphous material at high doses and low implantation temperature. (● 150 K, ■ 300 K, ▲ 473 K, ▼ 673 K, ◆ 760 K).

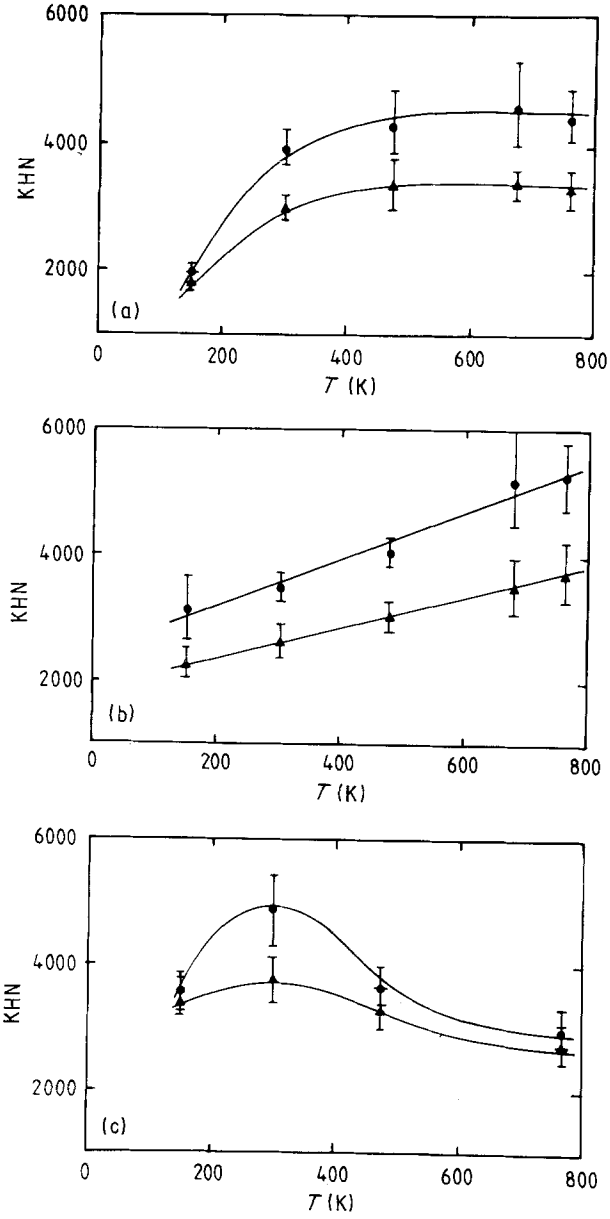

Figure 9 Variation of Knoop microhardness with implantation temperature for (1 0 $\bar{1}$ 2) sapphire implanted to (a) 2.5×10^{16} $Ti^+ cm^{-2}$ (b) 1.1×10^{16} $Y^+ cm^{-2}$ and (c) 1×10^{16} $Cr^+ cm^{-2}$. For all three implants the hardness increases from 150 to 300 K due to the annealing of the amorphous material formed by low temperature implantation. Above 300 K the hardness of the Ti-implant is approximately constant, whereas the hardness increases for Y and decreases for Cr implants. (● 25 g, ▲ 50 g).

amorphization dose has increased sufficiently that the maximum hardness occurs at around 1×10^{17} $Ti^+ cm^{-2}$. Similar results are observed for the Y-implanted sapphire specimens (Fig. 8a), though in this case the low dose, high temperature implants have a higher hardness than might be expected.

3.2.1.2. Explaining the hardness variations. Considerable success has already been achieved in modelling the hardness of implantation-induced structures containing amorphous material [1]. The increase in hardness with implantation temperature for 1.1×10^{16} $Y^+ cm^{-2}$ implantation (Fig. 9b) is, however, somewhat surprising. Increasing the temperature of implantation will increase the amount of annealing during the implantation process which might be expected to reduce, rather than increase, the hardness at higher implantation temperatures. The fact that the hardness of the 2.5×10^{16} $Ti^+ cm^{-2}$ implanted sapphire specimen is constant at implantation temperatures above 300 K (Fig. 9a) implies that any damage annealing in the damaged but crystalline material does not have a significant effect on hardness in the temperature range investigated here. Some temperature dependent hardening mechanism must occur for the Y-implants which is also implanted-ion specific. To check this, specimens were implanted with 1×10^{16} $Cr^+ cm^{-2}$ at temperatures in the range 150 to 760 K. For this ion, the specimen is amorphous at 150 K, but still crystalline above this temperature (as determined by electron channelling patterns). The hardness is a maximum at 300 K; it decreases slightly with temperature above this and decreases quite dramatically at lower temperatures (Fig. 9c). The low temperature decrease in hardness is due to amorphization, but, as with the Y-implant, the decrease at higher temperatures must be due to some other mechanism.

Comparing the results for these three ions gives some indication of the further mechanisms which

might be operating. One possible explanation for the observed hardness variations with both temperature and ion species comes from considering the size and charge state of the implanted ions and their possible contribution to solid solution hardening.

Suppose that increasing the temperature of implantation were to increase the amount of substitutionality of each of these ions with a commensurate reduction in interstitial – and presumed interstitial hardening – content, but an increase in substitutional hardening. The resultant solid solution hardening component then may or may not be greater than the initial damage-dominated hardening.

Existing solid solution hardening mechanisms for ceramics all assume that the solute ion is substitutional at a cation site within the solvent material. The potency of a particular substitutional solute ion for producing hardening is then known to be a function of both the solute–solvent ionic size mismatch and the effective charge state of the solute ion with local charge effects often being more important than mismatch strains [26].

Table VIII shows the nominal ionic radii of all the ions implanted in this study (data from [27]). It can be seen that the ionic radius of the Y^{3+} ion is much larger than Ti^{3+} which in turn is larger than Cr^{3+}. Thus, it might be expected that replacing Al^{3+} with Y^{3+} will produce the largest mismatch solid solution hardening effects in the absence of charge effects, while on this criterion, Cr^{3+} should produce very little hardening. This assumes that the ions are all substitutional to the same extent.

If it is further assumed that the ions will adopt the charge state determined by the local coordination (e.g. + 3 for Al in sapphire), then the further charge state contribution to solid solution hardening will not be particularly significant. If the solute ions are, however, present in their most thermodynamically stable charge state, then the charge state contribution to solid solution hardening, while still not significant for either Cr or Y (which as Cr_2O_3 or Y_2O_3 might be expected to form complete solid solutions in Al_2O_3 [28]), will be significant for titanium since Ti^{4+} is known to lead to considerable hardening of sapphire [26].

To counter this, Ti^{4+} ions are less likely to become substitutional than either Cr or Y and, indeed, extended X-ray absorption fine structure (EXAFS) studies of Ti-implanted sapphire [7] indicate that Ti is present in a range of charge states between + 2 and + 3 and thus some substitutionality but no significant hardening may occur. Since the observed hardness of Ti-implanted sapphire does not change much with temperature (as is observed above 300 K here), this suggests either that the Ti ions are not incorporated substitutionally or that they are incorporated as Ti^{3+}.

As shown earlier, the mechanism by which Y^{3+} produces hardening at high implantation temperatures could arise from the large size mismatch between Y^{3+} and Al^{3+}. In order for the Y^{3+} ion to become substitutional, a large misfit strain must be produced which may be reduced if cation vacancies become associated with the substitutional ions. Such solute–defect interactions will increase the effective charge state of the substitutional ion and would thus be expected to produce a strong solid solution hardening effect and an increase in surface hardness. Indeed EXAFS results indicate that the yttrium-doped sapphire has a tendency to be present in a charge state higher than + 3 [29] and hence may be associated with defects; thus, an increase in the amount of Y-substitutionality with temperature would explain the observed hardness behaviour.

Confirmatory evidence for these ideas is found in observations that the substitutionality of chromium implanted into sapphire increases with annealing temperature on post-implantation annealing [30]. RBS studies indicate that the increased substitutionality occurs at temperatures above 700 °C. This is somewhat higher than the substrate temperatures used here, but the presence of the "thermal spike" associated with the stopping ions is expected to significantly increase the effective temperature in the implanted layer and thus changes in substitutionality could occur. Further, the results of Farlow *et al.* [31] confirm that ions normally present in the trivalent state (Cr, Fe, Ga) show a greater tendency for substitutionality than those that are not normally trivalent (e.g. Ti, Ni). Titanium does show some partial substitutionality, but to a much smaller extent than chromium. Y^{3+} is known to act as an isovalent donor in sapphire [32] and so dislocation solute interactions (possibly of an electronic nature) may also be taking place in this case. Implantation-induced stress measurements (see next section) show that some damage annealing occurs as the implantation temperature is increased. If this were mostly the removal of interstitials to substitutional sites, then the small changes in stress could be explained since the volume expansion due to the implanted ions is only a small part of the total volume expansion responsible for the generation of stresses [8].

These results for sapphire demonstrate the subtle balance of effects contributing to hardening over and above radiation hardening. As the implantation temperature increases, Cr ions appear to be substitutionally incorporated into Al_2O_3 with charge state + 3 and these show little solid solution hardening because of the small size mismatch; Ti shows less substitutionality but may be incorporated in charge states other than + 3, with an overall small effect while Y is incorporated substitutionally but probably as a hardening defect complex of charge state other than + 3.

The behaviour of titanium implanted MgO is quite different and cannot be explained in a similar manner. The hardness against implantation temperature

TABLE VIII Nominal ionic radii of the implanted ions [27].

Ion species	Ionic radius (nm)
Al^{3+}	0.051
Cr^{3+}	0.063
Ti^{3+}	0.076
Ti^{4+}	0.063
Y^{3+}	0.089
Zr^{4+}	0.079

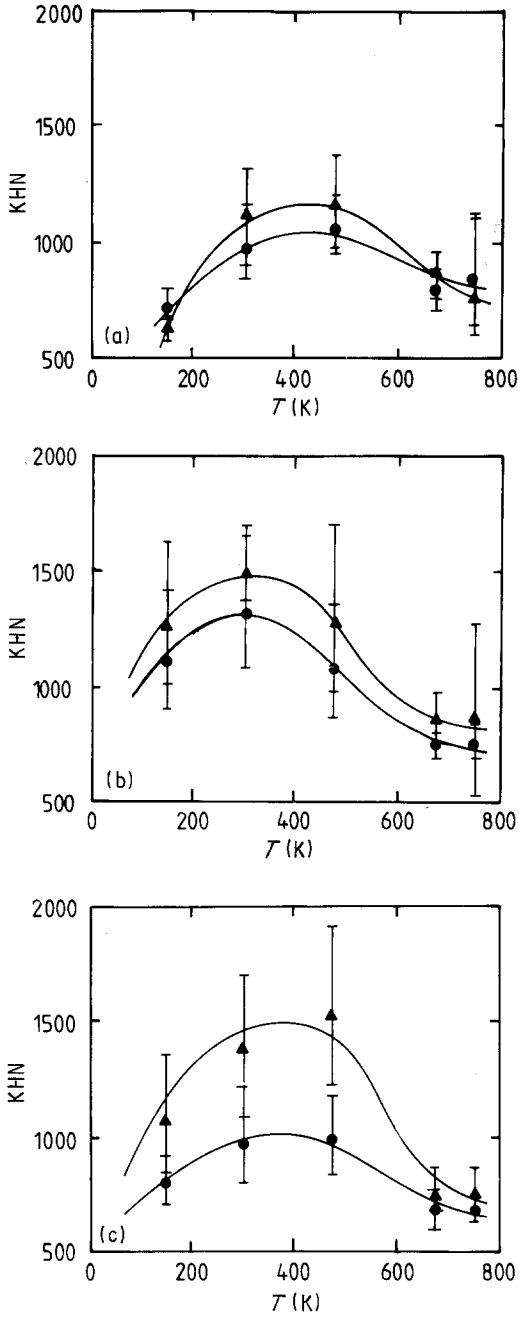

Figure 10 Variation of Knoop microhardness with implantation temperature for MgO implanted with (a) 1×10^{14} Ti^+ cm^{-2} (b) 1×10^{16} Ti^+ cm^{-2} and (c) 1×10^{17} Ti^+ cm^{-2}. The hardness increases from 150 K where the surface has become amorphized for all doses investigated, up to a maximum at between 300 and 473 K. Above this dose the hardness is reduced due to annealing of damage. (▲ 10 g, ● 25 g).

behaviour is shown in Fig. 10. For the specimen implanted to 1×10^{14} Ti^+ cm^{-2} the hardness increases up to a maximum at 473 K, above which it decreases until it is comparable with lower temperature implants. Similar behaviour is observed for implantation to the other two doses. At temperatures above 473 K some damage annealing occurs since the amorphization behaviour only affects the measured hardness below this temperature. The dose at which amorphization starts at 300 K is 8.5×10^{16} Ti^+ cm^{-2} by RBS and the hardness is observed to be reduced for implantation above this dose at 300 K. At lower temperatures the amorphization dose occurs somewhere between 1×10^{14} and 1×10^{16} Ti^+ cm^{-2}.

In summary, the measured hardness is critically dependent both on the occurrence of amorphization and the annealing of damage at high temperatures. Of these, the former is most important since the presence of soft amorphous material can dramatically reduce the hardness of the implanted layer. In the damaged but crystalline material, the balance between interstitial and substitutional solid solution hardening may also be playing a role and then considerations of ionic misfit and charge state will be important. It should, however, be realized that the vacancies created by the implantation process probably give the largest contribution to radiation hardening and cannot be ignored if the overall hardness levels are to be understood.

3.2.2. Implantation induced stresses

Fig. 11 shows the variation of integrated stress with substrate temperature for all the Ti-implanted sapphire specimens investigated in this study. For implantation to 2.5×10^{16} Ti^+ cm^{-2} the stress rises

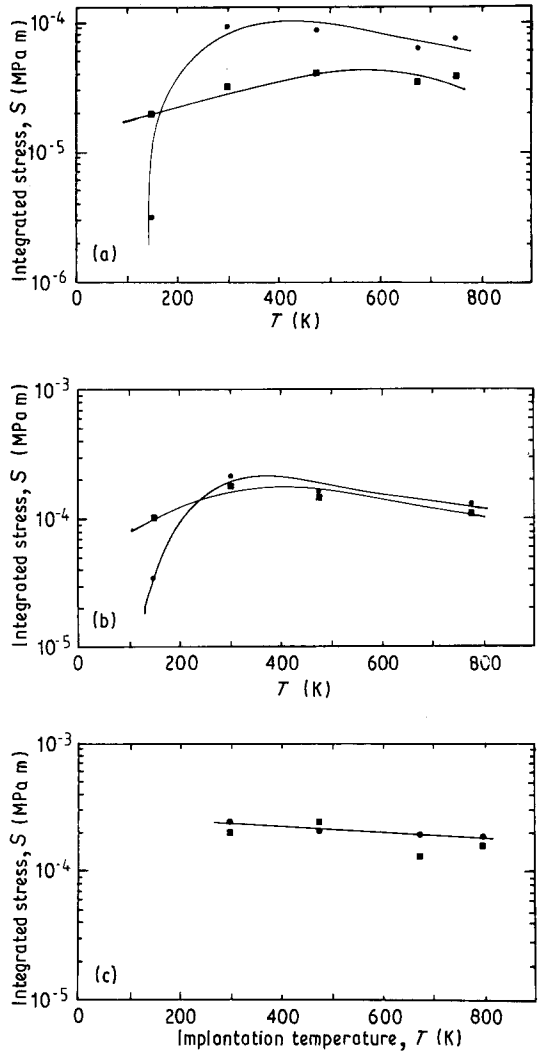

Figure 11 Variation of integrated stress (compressive) with implantation temperature for $(10\bar{1}2)$ sapphire implanted with (a) 2.5×10^{16} Ti^+ cm^{-2} (b) 1×10^{17} Ti^+ cm^{-2} (c) 7×10^{17} Ti^+ cm^{-2}. The presence of the thick amorphous layer at low temperatures gives marked stress relief. At higher temperatures the stress is reduced due to the annealing of implantation induced damage. For the high dose implants, the annealing of amorphous material also results in some stress relief (■ 500 g, ● 100 g).

from its lowest value for implantation at 150 K to a maximum for implantation between 300 and 473 K. At higher temperatures there is a small reduction in stress. Similar behaviour is observed for implantation to 1×10^{17} Ti^+ cm^{-2} except that the stress peak is closer to 300 K. For implantation to 7×10^{17} Ti^+ cm^{-2} it proved impossible to measure any stresses at 150 K (due to the effects of crazing – see Section 3.3.2) though above 300 K the stress decreases with increasing implantation temperature.

The low stresses measured for the 150 K implants are due to the presence of thick amorphous layers produced in the implantation of these specimens. Room temperature results have shown that considerable stress relief occurs on amorphization [8], indeed the relief of stress may contribute to the driving force creating amorphous material [3]. Stress relaxation has thus taken place in the amorphous material in the 150 K implants. At temperatures above 150 K, the stresses initially increase with temperature due to the reduction in the amount of stress relief given by the decreasing presence of amorphous material. Above 300 K the stresses are reduced presumably due to the annealing of some damage in the still crystalline regions. The removal of amorphous material at these higher temperatures might be expected to increase the measured stress due to a reduction in stress relaxation in the amorphous material. It appears, however, that sufficient damage annealing has taken place to counteract this. The increased substitutionality of the implanted atoms with increasing substrate temperature during implantation proposed in the previous section fits with the slight stress decreases observed with increasing temperatures in this regime.

The stresses produced in the high dose specimens (both 1×10^{17} Ti^+ cm^{-2} and 7×10^{17} Ti^+ cm^{-2}) are comparable and decrease at the same rate with temperature (Fig. 11b and c). This is evidence that the annealing process does not depend primarily on the detailed damage structure of the implanted layer, but mostly on the substrate temperature during implantation.

Fig. 12 shows the same plots for Y-implanted sapphire. For this material similar high temperature behaviour is observed (> 473 K) for all doses implanted; the stresses are annealed above this temperature and the annealing is more dramatic than for Ti-implanted sapphire. For the 1×10^{16} Y^+ cm^{-2} implant at 150 K no stresses could be measured, again due to stress relief in the thick amorphous layer on this specimen. At 300 K or above the stress behaviour is dominated by damage annealing. For the 9.9×10^{16} Y^+ cm^{-2} implanted specimen (Fig. 12b) the stresses increase with temperature up to 473 K. This is consistent with the amorphous layer thickness being reduced with temperature and the associated reduction in stress relief. A similar increase in stress is observed for implantation to 8.5×10^{17} Y^+ cm^{-2} (Fig. 12c). Here the increase is more marked than for the lower dose implant. There is a decrease in stress above 473 K for all doses but this is most marked for the samples implanted with 9.9×10^{16} Y^+ cm^{-2}. This is again evidence that some damage annealing occurs in the

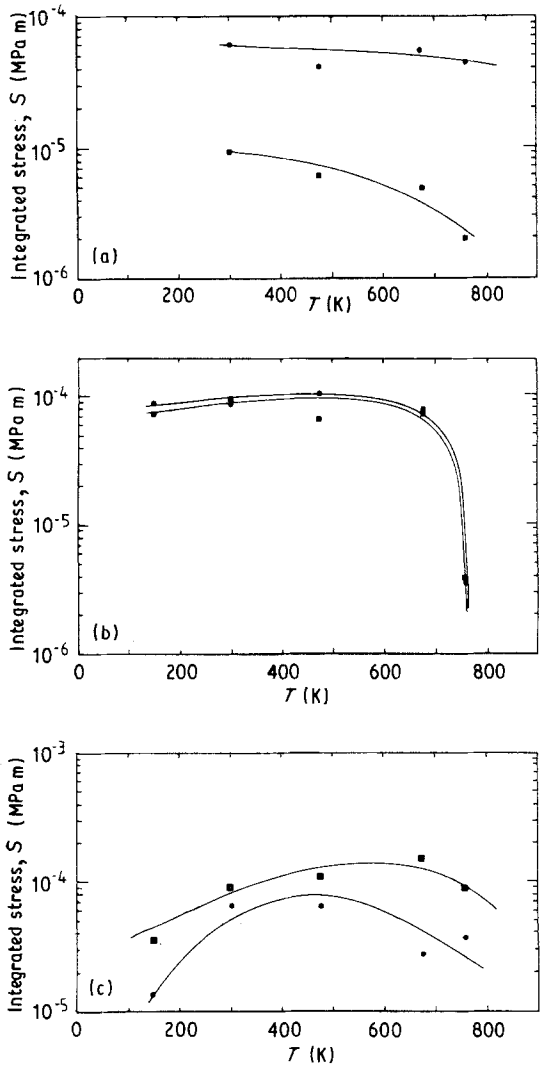

Figure 12 Plots of compressive integrated stress against implantation temperature for $(10\bar{1}2)$ sapphire implanted with (a) 1.1×10^{16} Y^+ cm^{-2} (b) 9.9×10^{16} Y^+ cm^{-2} and (c) 8.5×10^{17} Y^+ cm^{-2}. The formation of amorphous material at low implantation temperatures results in considerable stress relief. At higher implantation temperatures there is also some stress relief due to both the annealing of damage, and, at high implantation doses, the annealing of amorphous material. (■ 500 gf, ● 100 gf).

damaged but crystalline implanted layers as with the titanium implants though the amount of annealing is somewhat increased for these yttrium implants. The measured stresses in Fig. 12b and c are influenced by the presence of crazing and are thus much less accurate than the other stress measurements. Furthermore, there is evidence for the formation of yttrium aluminium garnet (YAG) in the implanted layer (see Section 3.2.3) which may lead to considerable stress relief. Indeed the samples implanted to 9.9×10^{16} Y^+ cm^{-2} at 760 K show the largest amount of YAG and no crazing due to the complete annealing of any amorphous material. The presence of this YAG probably leads to the low stresses measured for these samples (Fig. 12b).

After amorphization, the stress behaviour of the Y-implanted sapphire is affected by the presence of crazes in the surface layer of the material (see Section 3.3.2). Crazing produces further stress relief in the amorphous layer. The crazing phenomenon makes the measuring of cracks associated with indentations difficult and the craze structure often influences crack

paths and is thus likely to have an effect on the magnitude of the measured stresses. Crazing is a sensitive function of implantation temperature and thus is expected to arise as a function of the thermal stresses that are produced as a result of the heat generated by the implantation process. The extent of crazing varies across the implanted region being most pronounced at the centre of the implanted area and almost negligible near the implanted–unimplanted boundary which is further evidence that the thermal stresses due to temperature variations across the substrate are responsible for craze formation (see Section 3.3.2). Comparing heavily crazed regions and only partly crazed regions of the specimen implanted to 9.9×10^{16} Y^+ cm^{-2} at 300 K shows that the measured stresses in the two regions are very similar; thus, the stress relief associated with crazing is quite small and the damaged but crystalline material beneath the amorphous layer dominates the stress behaviour. This is in agreement with the results of Burnett and Page [8]. Indeed the stresses measured on specimens implanted to this dose at 300 K (where crazing is marked) and 473 K (where crazing is infrequent) are also comparable.

The stresses shown in Fig. 12 were checked by X-ray diffraction. The $(20\bar{2}4)$ diffraction peak was deconvoluted for α_1 and α_2 components and fitted with a Gaussian peak profile [41] which was used to determine the lattice parameter for both implanted and unimplanted materials. These were converted to internal stresses assuming a biaxial stress state [33]. The results were found to show the same trends as the stresses determined by the indentation method, but the integrated stress values determined were approximately an order of magnitude greater.

It can thus be seen that the damage-controlled implantation-induced stresses are a function of the implantation temperature and that they may be reduced both by amorphization and the annealing of damage.

3.3. Development of surface topography

3.3.1. Ti-implanted sapphire

For the Ti-implanted specimens no topographic features were found to develop after implantation for the majority of the implantation dose–temperature combinations. For implantation to 7×10^{17} Ti^+ cm^{-2} at 150 K, a heavily modified surface was, however, produced (Fig. 13). At this dose the peak Ti concentration is calculated to be $\sim$ 36 at % at 0.14 μm below the surface and the low implantation temperature will mean that this high concentration of titanium is accompanied by a very high damage concentration. It seems likely that considerable structural reorganization will thus have taken place in the amorphous layer. No new phase formation could be detected by X-ray diffraction, though a well defined $(20\bar{2}4)$ sapphire peak is obtained for implantation at 150 K which is missing at higher implantation temperatures (see Fig. 14). According to both electron channelling

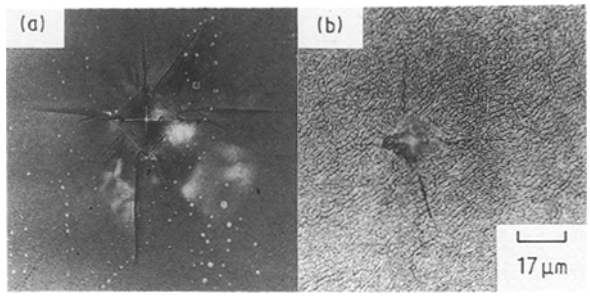

Figure 13 Reflected light micrographs of 500 g Vickers indents in the surface of $(1\,0\,\bar{1}\,2)$ sapphire implanted to (a) 2.5×10^{16} Ti^+ cm^{-2} (b) 7×10^{17} Ti^+ cm^{-2} at 150 K. The low dose implant shows no visible surface topography whereas the high dose implant shows increased surface roughness due to the formation of small crystallites in the amorphous layer.

ous layer. Fig. 15 shows a bright field TEM image of the implanted region in this specimen. Crystallites of $\sim$ 400 nm are clearly visible, but within these an array of smaller subgrains can be seen (of mean size 65 nm). If these are recrystallized areas that are randomly oriented within the larger crystallites with some amorphous material at the boundaries between them this would give a powder ring diffraction pattern with a superimposed amorphous ring diffraction pattern which could be indistinguishable from an amorphous pattern in the TEM and yet appear crystalline to X-rays due to the larger volume of crystalline material sampled. Similar subgrain structures have been observed in high dose ion implanted yttria stabilized zirconia [34].

Examination of the surface of this specimen by reflected light microscopy and SEM (Fig. 16) shows that it is also crazed. The craze network is superimposed on the arrangement of crystallites; some crazes can be seen to run between these. Since no other Ti-implanted specimen shows these features, the crazing phenomenon must be associated with the high damage levels. It appears that the crystallites have boundaries delimited by amorphous material; the boundaries between two different crystallite orientations may promote the nucleation of the crazes since the crystallites are separated by a film of weaker amorphous material which can also act as an easy crack path. Possible mechanisms for craze formation are discussed in the next section.

3.3.2. Y-implanted sapphire

The crazing phenomenon is a much more common occurrence in sapphire implanted with yttrium than with titanium or other species. Burnett and Page [2] commented on this but were unable to explain the origins of the crazing phenomenon other than by possible specimen bending leading to tensile tearing of the soft amorphous layer. Fig. 17 shows reflected light micrographs of the sapphire surfaces implanted with yttrium in this study. Also indicated is a line marking the boundary between crystalline and amorphous material. Crazes are also formed when amorphization has taken place. At 150 K a random array of crazes is

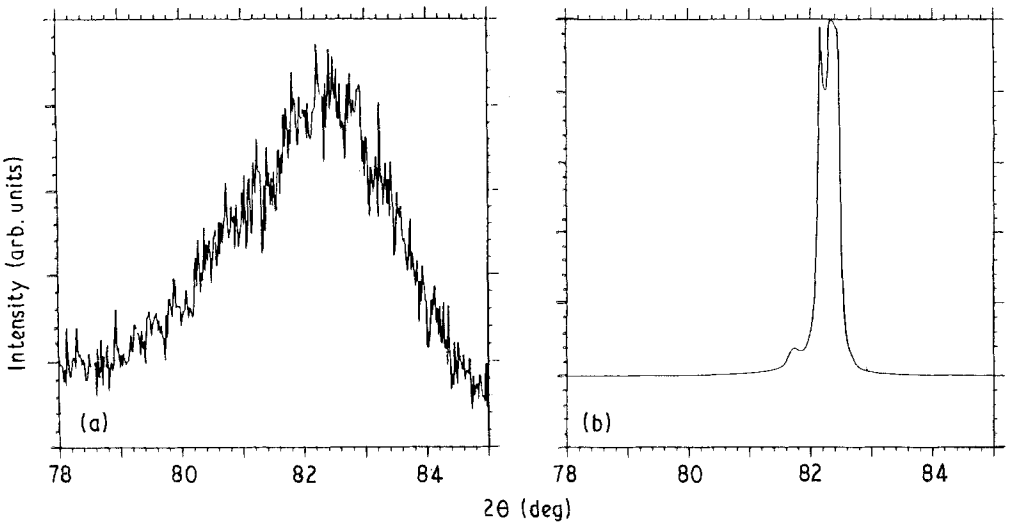

Figure 14 X-ray line profiles across the (20$\bar{2}$4) reflection in (1012) sapphire implanted to (a) 2.5×10^{16} Ti^+ cm^{-2} at 150 K (b) 7×10^{17} Ti^+ cm^{-2} at 150 K. The low dose implant shows a broad Gaussian peak characteristic of a thick surface amorphous layer, while the high dose implant shows a much sharper peak characteristic of a crystalline material [41].

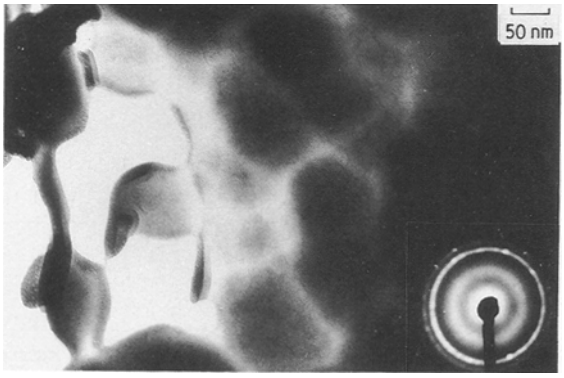

Figure 15 Bright field TEM micrographs of the amorphous layer in (1012) sapphire implanted to 7×10^{17} Ti^+ cm^{-2} at 150 K. The amorphous layer consists of an array of small ($\approx$ 50 nm) crystallites with smaller subgrains within them.

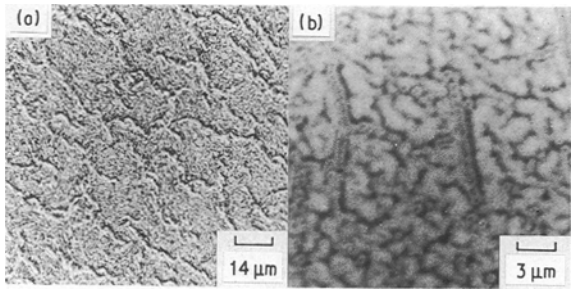

Figure 16 Showing the crazes within 7×10^{17} Ti^+ cm^{-2} implanted (1012) sapphire, implanted at 150 K (a) reflected light micrograph (b) secondary SEM micrograph. The crazes are broad tears in the heavily damaged amorphous layer.

above which are equivalent to the larger crazes seen for the Ti-implanted sapphire. At the higher dose there is also evidence for the cell-like subgrain structure as produced for the low temperature Ti-implant at the highest dose (Fig. 18). At 300 K fewer crazes are formed at both these doses, but the appearance of those crazes that do form is much the same. For implantation at 473 K no crazes form at 9.9×10^{16} Y^+ cm^{-2} and only a few form at the higher dose. The crazes that form at 673 K show a strongly crystallographic orientation; the crazes are oriented perpendicular to the trace of the (0001) plane reflecting the elastic anisotropy of sapphire ($E_\perp$ [0001] < $E_\parallel$ [0001] – 425 and 460 GPa, respectively) resulting in the maximum elastic strains in the substrate being perpendicular to the (0001) trace. As noted by Burnett and Page [2], this craze orientation precludes their origin being (0001) slip in the matrix. For the specimens implanted to 8.5×10^{17} Y^+ cm^{-2} at 760 K, only a few crazes are present because the amorphous layer has been mostly annealed at this implantation temperature.

None of the samples implanted in this study showed significant bending when investigated by surface profilometry and thus the simple explanation of Burnett and Page [2] seems inadequate. Further, the variation in crazing incidence and appearance with implantation temperature is evidence that some other temperature-dependent mechanism is operating.

3.3.3. Mechanism of craze formation

A new mechanism for the generation of crazes comes from considering the thermal expansion mismatch between the amorphous layer and the crystalline substrate. The thermal mismatch strain $\Delta\varepsilon$ generated between a material of thermal expansion coefficient α_b with a surface layer of thermal expansion α_s with an initial equilibrium temperature T_c is given by

$$\Delta\varepsilon = (\alpha_b - \alpha_s)(T_c - T_0) \quad (10)$$

where T_0 is the final temperature reached. This may be converted to a craze opening stress, σ (assumed to be biaxial in the surface) by

$$\sigma = \frac{E\Delta\varepsilon}{(1 - v)} \quad (11)$$

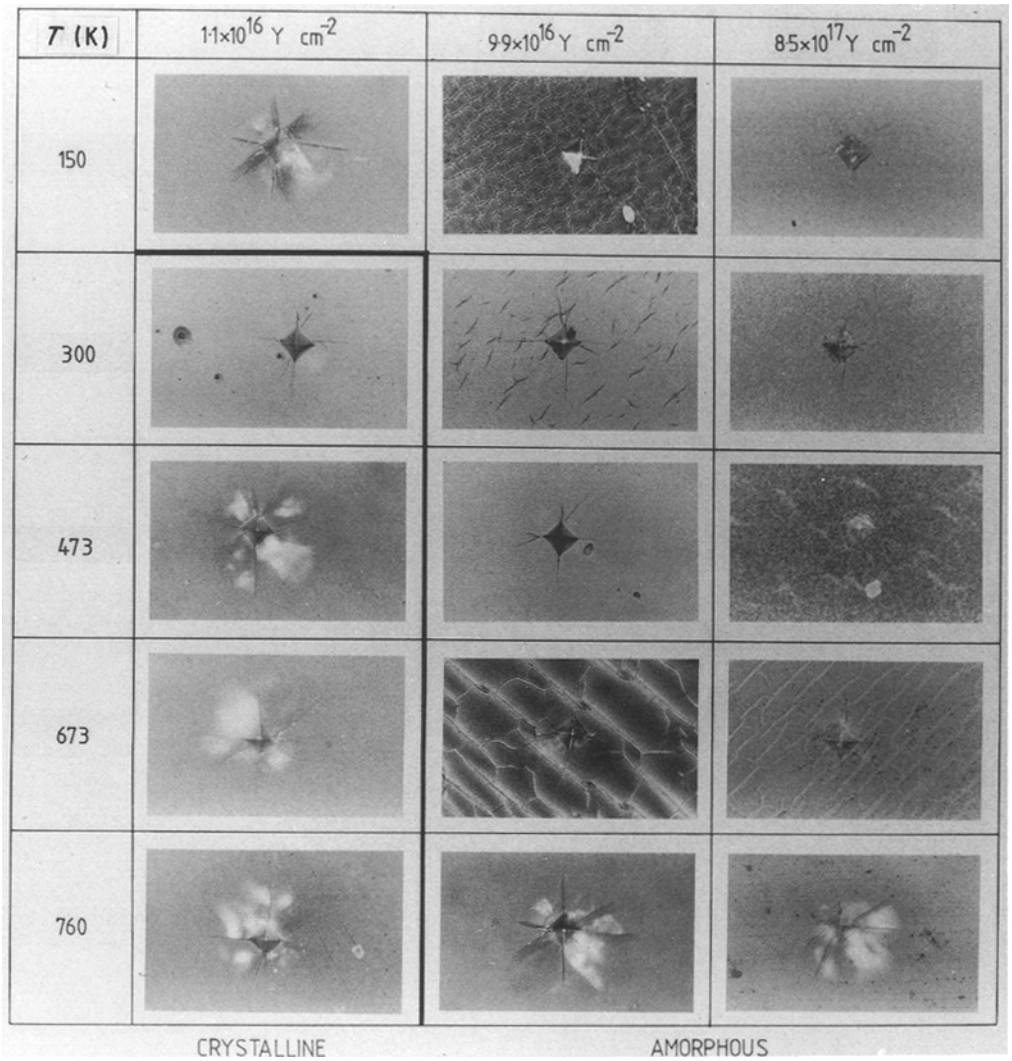

Figure 17 Showing the variation of surface topography with implantation dose and temperature for Y implanted (1 0 $\bar{1}$ 2) sapphire. Reflected light micrographs of 500 g Vickers indentations in each of the specimens implanted in this study. The boundary between amorphous and crystalline material is marked with a broad solid line. Note that visible crazes only form in materials where the amorphous layer extends to the surface.

where E is Young's modulus and v Poisson's ratio of the surface layer. This can be converted to an integrated stress by multiplying by the thickness of the amorphous layer.

Due to the effects of beam heating, the equilibrium temperature of both the amorphous layer and the substrate will be equal to the final specimen temperature reached during the implantation process. This is always greater than room temperature for the implants used here. At the end of implantation, when amorphization has occurred there thus will be no crazes present, but crazes will form on cooling the substrate back to room temperature. If tensile stresses are required for craze formation then α_s must be greater than α_b since $T_c > T_0$ in this case.

Fig. 19 shows the variation of α with temperature for Al_2O_3 [35] and Y_2O_3 [36]. Since the implanted layer will contain both Al–O and Y–O bonds the thermal expansion coefficient of the implanted material might be expected to be somewhere between the extremes denoted by these curves. The thermal expansion coefficient for a mixture of materials showing complete solid solubility is given by a simple method of mixtures [37]

$$\alpha_{ss} = \sum_i \alpha_i x_i \tag{12}$$

where α_i is the thermal expansion coefficient of the ith component and x_i its volume fraction. Most materials show slight deviations from this rule (e.g. [38]) but it provides a reasonable first approximation. The thermal expansion coefficient for an Al_2O_3–Y_2O_3 solid solution would thus lie between the extremes defined by the pure components. The thermal expansion coefficient against temperature plots for sapphire and Y_2O_3 cross at about 100 °C and thus two regimes of behaviour are expected. For materials that remain below the crossover temperature during implantation $(\alpha_s - \alpha_b) > 0$ and the thermal expansion mismatch strains generated on cooling will be tensile. Since α is also a function of temperature these strains will be given by

$$\Delta\varepsilon = \int_{T_0}^{T_c} (\alpha_s - \alpha_b) dT \tag{13}$$

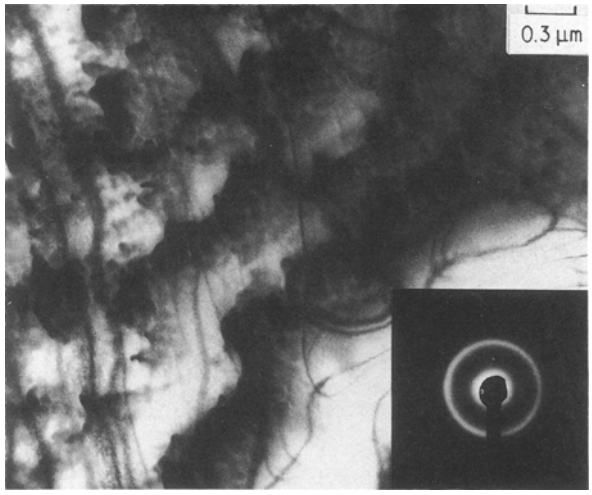

Figure 18 Bright field TEM micrograph of the surface of room temperature 8.5×10^{17} Y^+ cm^{-2} implanted $(1\,0\,\bar{1}\,2)$ sapphire. A similar crystallite structure to that produced by lower temperature high dose Ti implantation is produced.

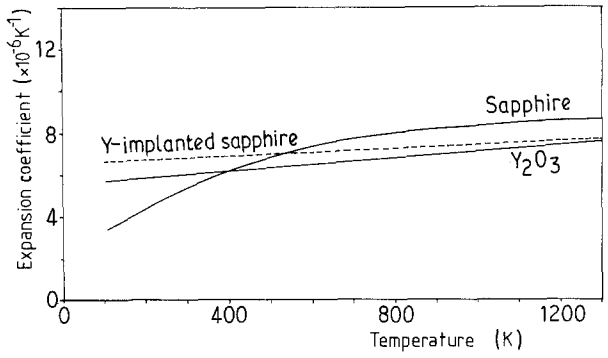

Figure 19 Variation of thermal expansion coefficient with temperature for sapphire and Y_2O_3. The thermal expansion coefficient of the implanted layer is expected to lie between these lines, however, due to the damage introduced by ion implantation (and the fact that the Young's modulus may be reduced by around 30%) the actual value may be somewhat higher as with the dotted line here.

In order that crazing can occur the tensile stresses produced on cooling must be greater than the implantation-induced compressive stresses.

The other region of behaviour occurs when the temperature of implantation is above the crossover temperature. In this case the thermal expansion mismatch stresses are compressive and may lead to failure of the implanted layer by buckling (see later).

In the case of the implanted layer, the crossover temperature may not be the same as given by simple solid solution arguments. As described in the previous section, there is some X-ray diffraction and TEM evidence for new phase formation at high doses in the Y-implanted sapphire specimens. The small crystallites that form on high dose implantation were found to contain highly strained yttrium aluminium garnet (YAG). This is the phase expected to be thermodynamically stable at this concentration of yttrium [30]. YAG is only found for substrates which have well developed amorphous layers and thus it is tempting to say that its formation requires a very large level of structural rearrangement such as occurs on amorphization. The thermal expansion coefficient of YAG is somewhat higher than that of any composition of Al_2O_3–Y_2O_3 solid solution; values $\sim 8.9 \times 10^{-6}\,K^{-1}$ over the temperature range of interest here have been quoted [39]. Thus the thermal expansion coefficient of the implanted layer is higher than given by solid solution behaviour and is estimated by the dotted line in Fig. 19.

Using Equation 13, $\Delta\varepsilon$ can be taken as the area between the implanted layer curve and the curve for sapphire in Fig. 19, bounded by room temperature at one end and the temperature at the end of implantation at the other. Maximum temperature values are quoted in Table I which give upper limits to the specimen temperature and so will give an upper limit to the thermal strains. For the room temperature implant, the temperature rise is $\sim 250\,°C$ and the maximum thermal mismatch strain estimated in this way is 2.5×10^{-4}. For Y-implanted sapphire this would result in a stress integrated over the amorphous layer of $(\sim 4\Delta x_d)$ $\sim 1.5 \times 10^{-5}\,MPa\,m^{-1/2}$ (using Equation 11 to calculate the stress with an amorphous layer thickness of ~ 100 nm). This is about an order of magnitude smaller than the implantation induced compressive stresses, but the discrepancies may be explained by a number of other factors.

Besides the formation of new phases, changes to the thermal properties of the implanted layer (including its thermal conductivity and emissivity) will be created during implantation as well as a temperature gradient between the bulk and the implanted layer. Crazing only develops on highly damaged materials and the presence of this damage is expected to reduce the thermal conductivity in the implanted layer. The heat dissipation from the thermal spikes by conduction to the bulk (and surface) will thus be reduced as implantation proceeds resulting in an increase in the temperature of the surface layer. This will increase the magnitude of the thermal expansion mismatch strains on cooling. Another effect of the damage would be to increase the thermal expansion coefficient of the implanted layer above the law of mixtures estimate since the damaged material is less strongly bonded.

A further important factor will be stress relaxation in the amorphous layer reducing the levels of implantation-induced stresses and thus allowing the tensile thermal expansion stresses to dominate: (the fact that crazing only occurs when amorphous material is present implies that the amorphous material is considerably mechanically weaker than its crystalline counterpart). Some such stress relief may be produced by the formation of the YAG crystallites. Burnett and Page [8] showed that the amorphous layer in Ti-implanted sapphire could support ~ 2 GPa implantation-induced stresses whereas the stresses supported by the Y-implanted layer were zero. This difference was attributed to stress relief due to the crazing process and probably has cause and effect reversed. In the light of the reappraisal presented here, it now seems likely that relief of implantation stresses is produced by the high damage levels associated with the implantation of a heavy ion (or low implantation temperatures) promoting the recrystallization or relaxation of part of the amorphous layer. For this

reason crazing is observed for the (heavier) Y-implants but not for the (lighter) Ti-implants in sapphire for room temperature implantation, though the thermal stresses would be larger for the Ti case.

It is the balance between these thermal stresses and the implantation-induced stresses which is thus responsible for crazing and, indeed, suggests another mechanism for craze formation.

For the case of Y-implanted sapphire, the expected thermal expansion mismatch behaviour shows two distinct regions with a crossover at $\sim 500\,^{\circ}C$ (using the dotted estimate for the expansion coefficient of the amorphous layer – see Fig. 19). At low temperatures the surface layer will expand or contract more than the substrate ($\alpha_s > \alpha_b$) and the thermal stresses generated on cooling will be tensile. Crazing, as described so far, is thus expected for all low temperature implants where the magnitude of these tensile thermal stresses is greater than the implantation-induced (compressive) stresses in the amorphous layer (which, themselves, may be close to zero). For implants that reach temperatures close to the crossover temperature the thermal expansion mismatch is small, but increases as the specimen cools down. Above the crossover point, where $\alpha_s < \alpha_b$, the initial thermal stresses will be compressive. As the specimen cools through the crossover, tensile thermal stresses are produced which counteract these compressive stresses (as well as the implantation induced stresses). There will, thus, be a temperature for which these high temperature compressive stresses balance the low temperature tensile stresses and no crazes will form. For the Y-implanted sapphire specimens the amount of crazing is dramatically reduced from implantation at 473 K compared to both higher and lower implantation temperatures (Fig. 17) so these specimens will have reached close to the temperature where there is a balance between the tensile and compressive stresses.

Specimens implanted at higher temperatures will have a compressive thermal expansion mismatch stress and, if compressive buckling is considered as well as tensile tearing, then two distinct types of craze are expected; those that form in response to tensile stresses at low implantation temperatures, and those that form in response to compressive stresses for high temperature implants. Indeed, two different types of craze are observed for Y-implanted sapphire depending on implantation temperature (Fig. 20). At low temperatures a random network of crazes is formed in response to the tensile thermal stresses, probably by tensile tearing of the amorphous layer. Crazes formed at higher temperatures show strongly crystallographic orientation and careful topographic examination by profilometry indicates that the edges of the crazes are raised. This is consistent with a craze formation mechanism resulting from the compressive buckling of the amorphous layer.

Surface profilometer traces across these crazes in $8.5 \times 10^{17}\ Y^+\ cm^{-2}$ implanted sapphire (room temperature implant – Fig. 21) reveal that the craze depth is about 113 nm (consistent with the craze extending right through the amorphous layer) and the craze width about 3.2 μm. Fig. 22 shows plots of craze width

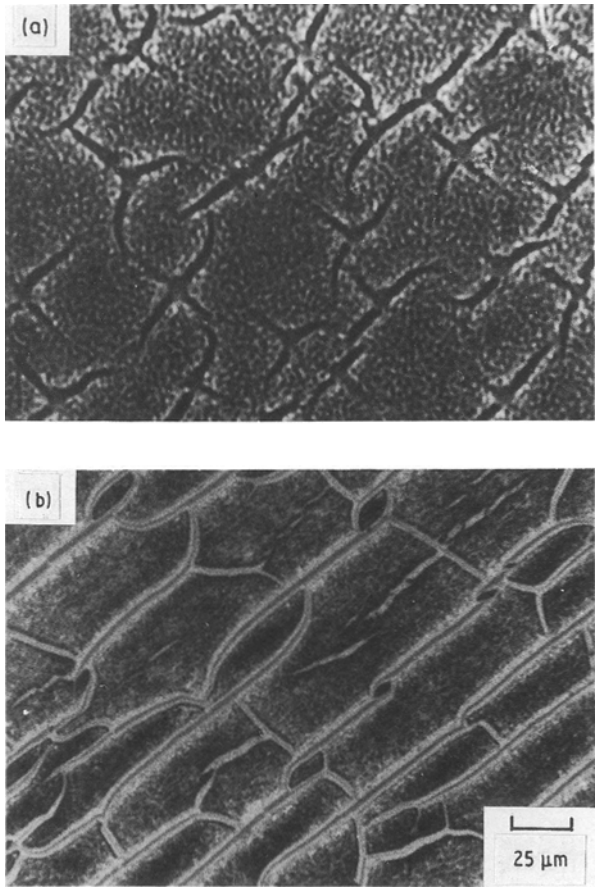

Figure 20 Reflected light micrographs showing the two distinct types of craze that form in yttrium implanted (1 0 $\bar{1}$ 2) sapphire. (a) A random network of crazes forms at low temperature. (b) At higher temperatures the crazes become more crystallographically oriented.

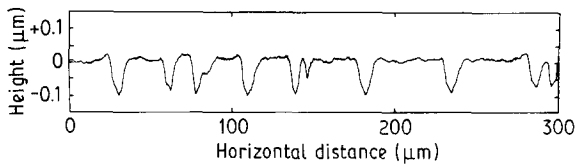

Figure 21 Surface profilometer trace across crazes in $8.5 \times 10^{17}\ Y^+\ cm^{-2}$ implanted (1 0 $\bar{1}$ 2) sapphire, implanted at 300 K. The crazes are $\approx$ 100 nm deep and penetrate down to the damaged but crystalline material beneath the amorphous layer.

and craze depth against implantation temperature. These are both minimum at about 473 K where the driving force for craze formation is smallest. It must be noted that the accuracy of these craze dimensions is limited by the radius of curvature of the tip of the profilometer stylus and thus the crazes are probably deeper than indicated in Fig. 22a due to their sharp tips.

In order to check the effects of thermal expansion on craze formation, a specimen implanted to $8.5 \times 10^{17}\ Y^+\ cm^{-2}$ at 673 K was heated in a vacuum furnace with a quartz window and the width of a particular craze was monitored *in situ* by reflected light microscopy during heating up to 840 °C and subsequent cooling to room temperature (Fig. 22). This was found to be reduced as the temperature was increased up to 500 °C. Above this it increases again until at 840 °C there was a rapid change in craze width accompanied by a change in appearance of

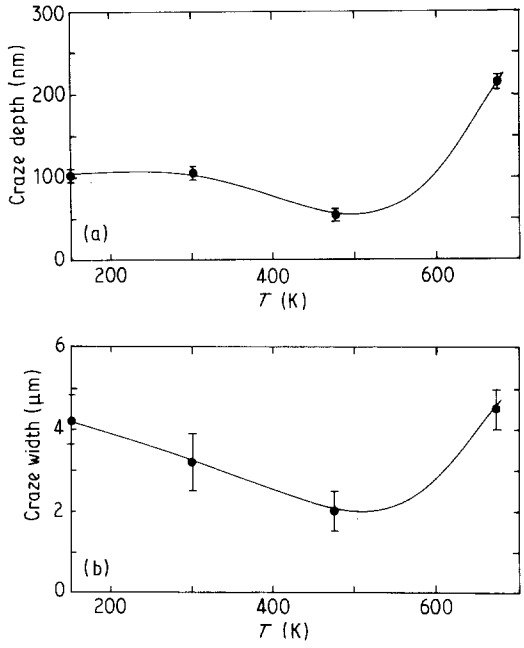

Figure 22 Plots of (a) craze depth and (b) craze width against implantation temperature for $8.5 \times 10^{17}\ Y^+\ cm^{-2}$ implanted $(1\,0\,\bar{1}\,2)$ sapphire. Both plots show a minimum at ≈ 473 K where it is close to the region where the thermal expansion coefficient of the implanted layer is the same as that of the bulk.

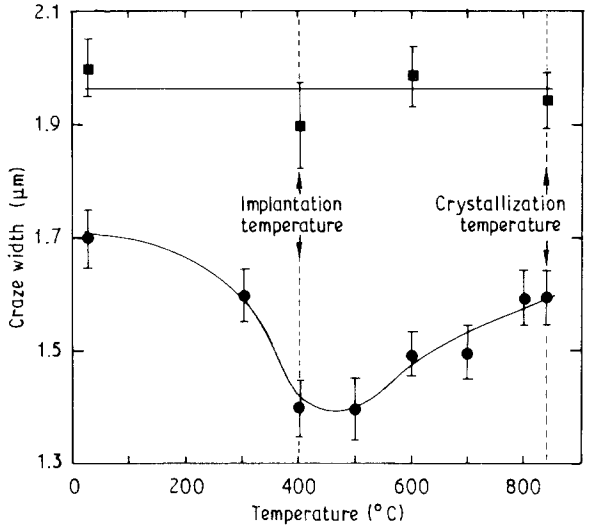

Figure 23 Plots of mean craze width against annealing temperature for $8.5 \times 10^{17}\ Y^+\ cm^{-2}$ implanted $(1\,0\,\bar{1}\,2)$ sapphire, implanted at 673 K. As the temperature increases, the craze width is reduced until it is minimum close to the implantation temperature. Above this temperature the craze width increases until at 840 °C there is a rapid increase in craze width corresponding to annealing of the amorphous layer. Once the amorphous layer is removed the craze width is virtually unaffected by reducing the temperature. (● T increasing, ■ T decreasing).

the amorphous layer. This is due to complete recrystallization of the amorphous layer; X-ray diffraction indicates that there is some formation of YAG, but the layer consists mostly of epitaxial sapphire. On cooling the crazes in the now recrystallized material do not change appreciably in width. The minimum in craze width is only around 100 °C above the temperature at which the substrate was held prior to implantation (and is close to the temperature rise measured for a room temperature implant).

On crazing the thermal stresses in the amorphous layer are relieved and thus on reheating the crazed material the crazes are expected to close up since the expansion coefficient of the amorphous material is greater than that of sapphire. This will happen up to the crossover temperature. Above this $\alpha_s < \alpha_b$ and the crazes will be opened up as the temperature is increased. If the crossover temperature for the implanted material–sapphire system was 500 °C, the observations reported here can be explained. It thus appears that the thermal expansion properties of the implanted layer play an important part in the craze formation process.

4. Conclusions

The effects of implantation on the implantation-induced structures formed in MgO and sapphire have been investigated using fluxes of Ti, Y and Cr ions and substrate temperatures in the range 150 to 800 K. Further the hardness and implantation-induced stresses in these samples have been determined and correlated with the implantation-induced structural changes. Four main areas of thermal sensitivity have been identified, namely

(a) The energy–dose threshold for amorphization varies with temperature such that amorphous structures can be produced at lower doses–energies at lower temperatures.

(b) The increased annealing expected in damaged-but-crystalline samples as the substrate temperature is increased has little effect on the total radiation hardening. Some changes in hardness are, however, observed which can be attributed to thermally sensitive changes in the substitutionality of the implanted ions.

(c) At high temperatures (> 600 K), dynamic recrystallization of the amorphous material occurs to produce new crystalline phases (such as yttrium aluminium garnet in the case of Y-implanted sapphire).

(d) Differential thermal expansion between the amorphous and undamaged material can lead to stresses causing crazing of the amorphous material, either by tensile tearing or compressive buckling of the damaged layer. These stresses are superposed upon the implantation-induced stress pattern which is usually compressive for ceramics and which, itself, may be modified by recrystallization, damage annealing or other stress relief mechanisms within the implanted layer.

Within these main areas a number of detailed conclusions may be drawn:

1. Amorphous layers are produced more readily (i.e. at lower implantation doses for a given ion energy–substrate combination) in both MgO and sapphire as the substrate temperature is reduced.

2. The amorphization threshold in terms of the critical energy deposition for amorphization (CECA) varies with temperature, rising as the temperature is increased. The variation with temperature is similar for both MgO and sapphire despite their different crystal structures but as might be expected if amorphization behaviour is dominated by ionicity considerations.

3. Analysis in terms of the Morehead and Crowder model [21] yields values for the activation energy for

the annealing of amorphous material at the edge of the displacement spike, U, of ~ 0.0018 eV which is extremely small compared to the activation energies for thermal annealing in normal conditions. This reflects the heavily damaged structure of the material and suggests that annealing is virtually athermal.

4. The variation of hardness as a function of implantation temperature depends on two factors, the presence of amorphous material and the differing solid solution effects of the implanted ions. Major increases in hardness can be measured for high dose implants where the amount of soft amorphous material is dramatically reduced as the implantation temperature is increased. Implantation of ions with different substitutionality, ionic misfit and effective charge state can lead to variations in the hardness of the damaged-but-crystalline material.

5. Implantation-induced stresses increase rapidly with implantation temperature if this is accompanied by a reduction in the amount of amorphous material produced. Otherwise the stresses decrease with increasing substrate temperature showing that some damage annealing occurs.

6. Crazes form as a result of the thermal expansion mismatch between the amorphous layer and the substrate. Different sorts of crazes are formed depending on whether the stresses produced are tensile or compressive.

7. For tribological applications, best properties (high hardness and improved crack resistance) are obtained for implantation at room temperature with good temperature control. Under these conditions implanted layers with maximum hardness and compressive implantation induced stresses are produced. Other properties such as adhesion [10, 40] are, however, also equally important and also vary with implantation temperature.

It can thus be seen that control of the temperature of the substrate during implantation is necessary if implanted layers with reliable properties are to be produced.

Acknowledgements

The authors wish to thank Professor D. Hull, FEng for the provision of laboratory facilities in Cambridge and Dr G. Dearnaley for the implantations at Harwell and useful discussions. TFP thanks Professor R. N. Parkins for research facilities at the University of Newcastle upon Tyne. SJB also wishes to acknowledge SERC and UKAEA Harwell for the provision of a CASE award.

Ms Muriel Emery and Ms Gail Hepple are thanked for preparing the manuscript.

References

1. P. J. BURNETT and T. F. PAGE, *J. Mater. Sci.* **19** (1984) 845–860.
2. *Idem., ibid.* **19** (1984) 3524–3545.
3. *Idem., Rad. Eff.* **97** (1986) 283–296.
4. C. J. McHARGUE, G. C. FARLOW, C. W. WHITE, J. M. WILLIAMS, B. R. APPLETON and H. NARAMOTO, *Mater. Sci. Eng.* **69** (1985) 123–127.
5. C. J. McHARGUE, *Nucl. Instrum. Meth.* **B19/20** (1987) 797–804.
6. T. HIOKI, A. ITOH, M. OHKUBO, S. NODA, H. DOI, J. KAWAMOTO and O. KAMIGAITO, *J. Mater. Sci.* **21** (1986) 1321–1328.
7. A. J. BOURDILLON, S. J. BULL, P. J. BURNETT and T. F. PAGE, *ibid.* **21** (1986) 1547–1552.
8. P. J. BURNETT and T. F. PAGE, *ibid.* **20** (1985) 4624–4646.
9. E. P. EERNISSE, *Appl. Phys. Lett.* **18** (1971) 581–583.
10. P. J. BURNETT and T. F. PAGE, *Inst. Phys. (London) Conf. Series*, **75** (1986) 789–802. (Proc. 2nd Int. Conf. Science of Hard Materials, Rhodes, 1984).
11. S. J. BULL and T. F. PAGE, *J. Mater. Sci.* **23** (1988) 4217–4230.
12. P. J. BURNETT and T. F. PAGE, in "Plastic Deformation of Ceramic Materials II", edited by R. C. Bradt and R. E. Tressler (Plenum, New York, 1984) pp. 669–680.
13. *Idem., Mater. Res. Soc. Symp. Proc.* **27** (1984) 401–406.
14. G. DEARNALEY, J. H. FREEMAN, R. S. NELSON and J. STEPHEN "Ion Implantation" (North Holland, Amsterdam, 1973).
15. P. D. PARRY, *J. Vac. Sci. Technol.* **13** (1076) 622–629.
16. I. MANNING and G. P. MUELLER, *Comput. Phys. Commun.* **7** (1974) 85–94.
17. D. C. JOY, D. E. NEWBURY and D. L. DAVIDSON, *J. Appl. Phys.* **53** (1982) R81–R122.
18. T. F. PAGE, C. J. McHARGUE and C. W. WHITE, *J. Microsc.* (1991) in press.
19. B. R. LAWN and E. R. FULLER, *J. Mater. Sci.* **19** (1984) 4061–4067.
20. G. R. ANSTIS, P. CHANTIKUL, B. R. LAWN and D. B. MARSHALL, *J. Amer. Ceram. Soc.* **64** (1981) 533–538.
21. F. F. MOREHEAD and B. L. CROWDER, *Rad. Eff.* **6** (1970) 27–32.
22. J. H. CRAWFORD, *Nucl. Instrum. Meth.* **B1** (1984) 159–165.
23. J. C. BOURGOIN, J. F. MORHANGE and R. BESERMAN, *Rad. Eff.* **22** (1974) 205–208.
24. H. M. NAGUIB and R. KELLY, *ibid.* **26** (1975) 1–12.
25. L. A. CHRISTEL, J. F. GIBBONS and T. W. SIGMON, *J. Appl. Phys.* **52** (1981) 7143–7146.
26. T. E. MITCHELL and A. H. HEUER, *Mater. Sci. Eng.* **28** (1977) 81–97.
27. R. C. WEAST (ed), "Handbook of Chemistry and Physics" (Chemical Rubber Company Press, Columbus, OH, 1983).
28. E. M. LEVIN and H. E. McMURDIE, "Phase Diagrams for Ceramists: 1975 Supplement" (American Ceramic Society, Columbus, OH, 1975).
29. M. K. LOUDJANI, J. ROY and A. M. HUNTZ, *J. Amer. Ceram. Soc.* **68** (1985) 559–562.
30. H. NARAMOTO, C. W. WHITE, J. M. WILLIAMS, C. J. McHARGUE, O. W. HOLLAND, M. M. ABRAHAM and B. R. APPLETON, *J. Appl. Phys.* **54** (1983) 683–698.
31. G. C. FARLOW, C. W. WHITE, C. J. McHARGUE and B. R. APPLETON, *Mater. Res. Soc. Symp. Proc.* **27** (1984) 395–400.
32. M. M. EL-AIAT and F. A. KROGER, *J. Amer. Ceram. Soc.* **65** (1985) 280–283.
33. T. I. KAMINS and E. S. MEIERAN, *J. Appl. Phys.* **44** (1973) 5064–5066.
34. A. J. BURGGRAAF, D. SCHOLTEN and B. A. van HASSEL, *Nucl. Instrum. Meth.* **B32** (1988) 32–36.
35. B. YATES, R. F. COOPER and A. F. POJUR, *J. Phys. C* **5** (1972) 1046–1058.
36. D. W. STACEY and D. R. WILDER, *J. Amer. Ceram. Soc.* **56** (1973) 224.
37. D. MEGAW, *Mater. Res. Bull.* **6** (1971) 1007–1018.
38. J. E. SHELBY, *J. Appl. Phys.* **47** (1976) 4489–4496.
39. T. K. GUPTA and J. VALENTICH, *J. Amer. Ceram. Soc.* **54** (1971) 355–356.
40. S. J. BULL and T. F. PAGE, *Nucl. Instrum. Meth.* **B32** (1988) 91–95.
41. B. E. WARREN, "X-ray Diffraction" (Addison-Wesley, Reading, MA, 1969).

Received 9 August
and accepted 4 September 1990